Tensorial formulations for improved thixotropic viscoelastic modeling of human blood

Matthew Armstrong[1,a], Andre Pincot[1], Soham Jariwala[2], Jeff Horner[2,3], Norman Wagner[2], and Antony Beris[2]

AFFILIATIONS
[1]Department of Chemistry and Life Science, Chemical Engineering Program, United States Military Academy, West Point, NY 10996
[2]Center for Research in Soft Matter and Polymers, Department of Chemical and Biomolecular Engineering, University of Delaware, Newark, DE 19716
[3]Thermal/Fluid Component Sciences Department, Sandia National Laboratories, Albuquerque, NM 87123

[a]Author to whom correspondence should be addressed; electronic mail: matthew.armstrong@westpoint.edu

Abstract

Recent work modeling the rheological behavior of human blood indicates that blood has all the hallmark features of a complex material, including shear-thinning, viscoelastic behavior, a yield stress and thixotropy. There is renewed interest in the modeling of human blood with thixo-elasto-visco-plastic rheological models. Previous work [Armstrong and Tussing, Phys. Fluids 32, 094111 (2020)] has led to the development of the enhanced thixotropic viscoelastic model for blood (ethixo-mHAWB; called here, after a minor modification, ETV) that incorporates viscoelasticity to a thixotropic model for the stress contributed by the rouleaux aggregates, in addition to describing using a nonlinear viscoelastic model the stress contributed by the individual red blood cells deforming under the action of the flow. This model has shown superior performance in fitting human blood steady state and transient rheological data from a strain-controlled rheometer [Horner et al., J. Rheol. 62, 577-591 (2018) & 63, 799-813 (2019)] as compared to other alternate models. In the present work, we first develop another variant of the ETV model, the enhanced structural stress thixotropic-viscoelastic model (ESSTV), the modification patterned following an elastoviscoplastic model developed recently [Varchanis et al., J. Rheol. 63, 609-639 (2019)]. We develop full tensorial stress formulations of the rouleaux stresses for both the above-mentioned models, resulting in the t-ETV and t-ESSTV models. We use steady state and step-ups, and step-downs in shear rate data to independently fit the parameters of all before-mentioned models. We compare predictions against experimental data obtained on Small, Large, and Unidirectional Large Amplitude Oscillatory Shear (SAOS, LAOS and UDLAOS) conditions. We find that the full tensor stress formulations t-ETV and t-ESSTV significantly improved the predictive capability of the earlier ETV model.

Key words: thixotropy – viscoelasticity – plasticity – elasticity

I. INTRODUCTION

Within human blood's aqueous plasma, we find suspended a variety of proteins and cells. The latter involve the three most vital components of blood: platelets, red blood cells (RBCs), and white blood cells. The suspended RBCs, when left at rest or under a low shear rate, form into structures resembling coin stacks, dubbed "rouleaux." The formation of these rouleaux is generally dependent upon the stress and/or shear rate as well as on the concentration of various plasma proteins such as fibrinogen [1,2]. The destruction and formation of rouleaux are reversible, depending on the magnitude of shear rates [3].

As rouleaux form, they collectively act to increase the viscosity of blood, contributing a portion of its complex flow properties that include viscoplasticity, viscoelasticity, and thixotropy [4-7]. Viscoplasticity refers to the existence of a non-zero yield stress below which the material deforms elastically but above which it flows undergoing permanent, irreversible deformation. Viscoelasticity indicates the simultaneous presence of viscous and elastic characteristics, and thixotropy describes a fluid's time-dependent decrease of viscosity under shear *deformation* tied to microstructure. Blood's viscoplasticity and thixotropy are due to the formation and subsequent under flow destruction of the rouleaux aggregates. As the intermolecular forces present in rouleaux are quite weak, blood's yield stress is generally low, rarely exceeding a magnitude of 1 – 4 mPa [8-10]. Given the high concentration of RBCs, the rouleaux combine into network structures that also provide part of the viscoelastic blood characteristics. An additional viscoelasticity exists contributed by the elastic deformation of individual RBCs suspended in plasma [8-9].

The viscoelastic response, and other complex behaviors of blood from the rouleaux is primarily encountered at low shear rates, generally, below 10 s^{-1} [10]. In contrast, the viscoelasticity resulting

from the flow-induced deformation of individual RBCs corresponds to shorter relaxation times resulting at steady state to a viscosity that exhibits significant shear thinning at shear rates within $10 - 1000\ s^{-1}$ [8, 11-16]. This behavior necessitates the design of more sophisticated constitutive models combining thixotropy and at least two modes of viscoelasticity to effectively model in-vivo blood flow.

Due to the relevance of hemorheology in enhancing current understanding of blood and pathology prevention, detection, and treatment, the development of the discipline has become of particular interest [17-20]. Yet, as useful as these applications of hemorheology may be, they all require robust methods by which to collect data and subsequently simulate the in-vivo phenomena accurately, including the more complex aspects of blood's transient behaviors. The simulations provided by such models are vital in efforts to engineer more sophisticated medical equipment and treat debilitating conditions of the vasco-circulatory system [21]. Moreover, as one of the most evidently relevant thixotropic fluids, continued study of blood's properties and behaviors within the body can be prosecuted using a few thixotropic models developed within the recent past.

Blood rheology models have undergone several refining evolutions, beginning with simple, generalized Newtonian, models, such as the Casson, Carreau-Yasuda, and Herschel-Bulkley models [22, 23]. All these adequately represented most aspects of steady state flow behavior, including shear thinning and, depending on the specific model, yield stress. However, these models fail to predict correctly the transient rheological behavior of blood, due to thixotropy and the fact that human blood has two viscoelastic timescales: one viscoelastic timescale for the plasma and individual RBC; and the second viscoelastic timescale for the evolving rouleaux. These are key features, as mentioned above, of blood rheology that in part arise from a history-dependent microstructure that also provides for yield stress and viscoelasticity of the rouleaux. Therefore,

modern models have come to include additional features that allow for a more faithful prediction of, and agreement with the experimentally measured transient rheological response [8, 9].

Viscoelasticity is typically modelled phenomenologically through modifications of the Maxwell, Giesekus and Oldroyd-8 constant frameworks [24-26], which are generally sufficient to model the transient behavior at high shear. However, these models are unable to effectively replicate the transient behavior of blood at lower shear rates where blood proves far more dynamic [7-10]. The simple fact is some non-thixotropic models can sometimes capture some of the rheological behavior, for some experiments. However, to capture all the nuanced, and complicated rheological behavior of human blood for all the rheological experiments we show requires a model that has a thixotropic component that has three things: 1. A timescale of shear rouleaux breakage; 2. A timescale of shear rouleaux reformation; and 3. A timescale of Brownian rouleaux reformation. Our thixotropic framework has all three. To address this low shear behavior, a more rigorous thixotropic model is necessary. A component of a standard thixotropic model incorporates a kinetic rate equation that governs the time evolution of a nondimensional structure parameter varying between 0 and 1, with 0 indicating a complete lack of structure and 1 representing a full structure [27-30]. Yet, the viscoelastic nature of blood requires either the incorporation of microstructure-dependent elasticity through the addition of dual elastic and plastic stress terms or the integration of the structure parameter into a generalized viscoelastic model [31-32].

The terms of elasticity and plasticity can be defined through the separation of total strain and its time derivative (total strain rate) into two components [28, 31, 33]. The plastic behavior can be modeled after the kinematic hardening theories of plasticity [33], further separating into isotropic hardening (IH) and kinematic hardening (KH) [34, 35]. More than just affecting plasticity, the IH of a material refers to how the internal dimensionless structural parameter is

related to its thixotropic properties whereas KH describes the deformation-dependent effective yield stress [33-35]. Also, Wei et al. developed the ML-IKH model to provide a spectrum of lambda values, with independent thixotropic time scales of evolution, combined with isotropic kinematic hardening [36]. Following a parallel approach, Varchanis et al. [37] developed the SPTT-IKH model, where the *'S'* refers to the plasticity term, first introduced by Saramito [31], and the *'PTT'* refers to the Phan-Thien Tanner model for viscoelastic fluids [38]. These models were all cast in tensorial form and contained from 11 – 15 parameters. IH and KH play a vital role in the dynamics of fluid systems, necessitating inclusion of representative equation parameters. KH phenomena can also act to induce lag between back stress evolution and shear stress [33-37].

A simplified form of kinematic hardening has been introduced already into the earliest of the thixotropic models in our group [39]. It was clear from this work though that the limitation for testing the applicability of the model was the lack of sufficiently detailed transient experimental data. That changed in the subsequent years with a slew of data, obtained under carefully controlled conditions and based on rigorous guidelines [40] under a variety of transient conditions that allowed for a substantial extension of the early thixotropic model [8]. The data covered in addition to steady state a systematic variation on both the amplitude and frequency in Unidirectional Large Amplitude Oscillatory Shear (UD-LAOS) generated from the superposition of a steady and oscillatory shear so that the lowest applied shear rate is zero, and never negative. Those data, along with powerful model parameter estimation approach, based on a stochastic global optimization approach (parallel tempering) [41], allowed for a significant enhancement of the thixotropic model for blood. A significant new contribution was the representation of the deformable RBC viscoelasticity using a generalized White-Metzner-Cross model, leading to a thixotropic viscoelastic model (TVM—which we called in the past as HAWB model) [8]. A further extension

of TVM was achieved shortly afterwards that led to a substantial better fit of the transient data by allowing for the introduction of a rouleaux viscoelastic response, the mHAWB model [9]. This last model has also appeared in recent publications (as ethixo-mHAWB) with small modifications of the kinetic equation to incorporate a shear aggregation term for the structural parameter. It is also used here with one further small modification, calling it, better reflecting its physical nature, the enhanced thixotropic viscoelastic (ETV) model [9, 42].

More recent work attempted to investigate closer the role of different rheological model components. More specifically, Armstrong and Tussing [10] and Armstrong and Pincot [43] investigated if there was any advantage to describe the deformed RBCs using a general Oldroyd-8 model [24] or a Giesekus model [44], respectively, instead of the generalized White-Metzner-Cross model as in the mHAWB model (there was not). In contrast to this work, and ignoring the viscoelasticity of the deformable RBCs, Armstrong et al. [45], tried to develop better models for blood rheology by following the elastic modifications to a viscoplastic (Herschel-Bulkley) model proposed by Saramito [31] and using his ideas resulting in the ethixo elastoviscoplastic (ethixo EVP) models, on which they introduced thixotropy through a structural parameter obeying a kinetic equation, thus generating thixoelastoviscoplastic (TEVP) descriptions [45]. They developed several TEVP variants depending also on the starting EVP model and showed that the introduction of thixotropy helps fitting the transient experimental blood rheological data better. The opposite approach, i.e., the addition of viscoelasticity to a viscoplastic and thixotropic model, such as the model developed in [39], has also been tried and shown to lead to better fits to experimental transient blood rheology data [42, 47, 48]. Interestingly, Armstrong et al. [47] incorporated a viscoelastic timescale of evolution to the contribution to total stress from rouleaux to the original Modified Delaware Thixotropic Model (MDTM). This enhancement was given the

moniker: VE-MDTM, viscoelastic enhanced MDTM. This modification clearly demonstrated that there is in fact a unique viscoelastic timescale of the stress from the evolution of the rouleaux to the total stress. A similar approach has been followed by Giannokostas et al. [48] modifying the Varchanis et al. model, which was the SPTT-Isotropic Kinematic Hardening [37] TEVP model, to better fit blood rheology.

The involvement of separate timescales for thixotropic and viscoelastic fluid response, along with complementary shear structure breakage and structure build-up timescales, affords so far, the best capability to precisely model the rheological behavior of blood and its component rouleaux microstructures (ethixo-mHAWB model) [9, 42]. While the addition of more parameters to a model is not ideal as they entail additional complexity, the thixotropic and viscoelastic timescales offer additional insight into the gradual evolution of rouleaux within the bloodstream. Enhanced, accurate models then act to facilitate the use of CFD modeling for more efficient analysis of blood properties.

While the ethixo-mHAWB model has proven more successful in fitting available steady state and especially transient rheological data for blood than other models and variants it has not been perfect [10, 43]. Thus, more effort is warranted in trying to further improve it. We start here with a simplification to the ethixo-mHAWB model, by replacing the plastic component of the strain rate with the total strain rate in the equation describing the viscoelastic contribution of the Rouleaux stress, resulting in what we call here the Enhanced Thixotropic Viscoelastic (ETV) model. This is a slight modification, introduced for facilitation of further changes to the ETV model, and hardly affects its predictive capabilities. Our basic contributions are two more substantial modifications. First, we modify the ETV model by adopting a novel viscoelastic-elastic formulation to express both the elastic and viscoelastic stress contributions of blood rouleaux

microstructures, using recently published theories of plasticity [31, 37]. This modification, results in a model that we call Enhanced Structural Stress Thixotropic Viscoelastic (ESSTV). Second, we transform to a full stress tensor description the viscoelastic contribution and total stress contribution, from the rouleaux in both the ETV, and the new ESSTV models, resulting into the t-ETV and t-ESSTV models, respectively. All models are described in Section II. Within Section III, for each model, the parameters are determined based on least squares fit against steady state and transient shear data, using an efficient stochastic global optimization approach based on parallel tempering developed in previous work [41]. For each model, a subset of the model parameters is determined through a fit to a set of existing steady state simple shear flow data. The rest of the model parameters are then determined by a simultaneous fit of a series of three step-ups in shear rate, and three step-downs in shear rate experiments. Using these model parameters, in Section IV we compare the ability of the new models to accurately predict small amplitude oscillatory shear (SAOS), large amplitude oscillatory shear (LAOS) and unidirectional large amplitude oscillatory shear (UDLAOS). In Section V, the conclusions from this study are offered.

II. MODEL BACKGROUND AND FRAMEWORK

Moving forward the Model and Background and Framework section is organized as follows: a description of the Enhanced Thixotropic Viscoelastic (ETV) model; and then a description of the Enhanced Structural Stress Thixotropic Viscoelastic (ESSTV) model. From here the tensorial descriptions are discussed with summary tables provided for full tensorial versions of the models. The goal is to introduce the enhanced models, and describe the parameters, algebraic and differential equations of each.

II.1 ETV Model

The ETV model arose from the original work of Horner and coworkers (as the HAWB [8] and then mHAWB [9] models) and it was further modified by Armstrong and Tussing [10] (as e-thixo-mHAWB). It is introduced here with a further simplification as ETV model. The simplification, as explained below, alters little to the predictive capabilities of the original e-thixo-mHAWB model. The model is described currently for a shear flow in a Cartesian system of reference x,y,z with x the flow direction, y the shear direction and z the neutral direction. The central component of the ETV model is that the total shear stress, σ_{xy}, arises as the superposition of three independent contributions: 1) a viscoelastic contribution due to red blood cells deformation suspended into plasma, $\sigma_{C,xy}$, 2) a viscoelastic contribution due to the red blood cell aggregation into rouleaux structures, $\sigma_{V,xy}$ and 3) an elastic contribution due to the rouleaux, $\sigma_{E,xy}$:

$$\sigma_{xy} = \sigma_{C,xy} + \sigma_{V,xy} + \sigma_{E,xy} . \tag{1}$$

The starting point for the description of the viscoelastic response of the individual deformable RBCs is a White-Metzner model [50] that incorporates the Cross model [51] for the shear viscosity $\eta_C(\dot{\gamma})$ as follows

$$\boldsymbol{\sigma}_C + \frac{\eta_C(\dot{\gamma})}{\mathrm{G}_C} \overset{\nabla}{\boldsymbol{\sigma}}_C = \eta_C(\dot{\gamma})\dot{\boldsymbol{\gamma}} \text{ , and} \tag{2}$$

$$\eta_C(\dot{\gamma}) = \mu_{C\infty} + \frac{(\mu_{C0} - \mu_{C\infty})}{(1+\tau_C\dot{\gamma})} . \tag{3}$$

where G_C is the elastic modulus, $\dot{\boldsymbol{\gamma}}$ is the rate of strain tensor, and τ_C is the Cross model time constant, and μ_{C0} and $\mu_{C\infty}$ are zero and infinite individual RBC viscosity, respectively. In Eq. (2)

the superimposed inverse triangle, $\overset{\nabla}{}$, denotes the upper-convected time derivative defined as follows [25]

$$\overset{\nabla}{\boldsymbol{\sigma}} \equiv \frac{\partial}{\partial t}\boldsymbol{\sigma} + \mathbf{v}\cdot\nabla\boldsymbol{\sigma} - \boldsymbol{\sigma}\cdot\nabla\mathbf{v} - \nabla\mathbf{v}^{\mathrm{T}}\cdot\boldsymbol{\sigma}, \tag{4}$$

where $\mathbf{v}$ is the fluid velocity and $\nabla\mathbf{v}$ is the velocity gradient, $(\nabla\mathbf{v})_{ij} = \partial v_j / \partial x_i$, $x_1 = x, x_2 = y, x_3 = z$.

To avoid potential instabilities [26] and following the work of Souvaliotis and Beris [52] extending the White-Metzner model, Horner and coworkers recast the previous equation using the first invariant of the stress tensor as the parameter to the viscosity function [8, 9]. Expressed in terms of the stress components in the *xy* and *xx* direction the full equations for shear flow are [8, 9] (after correcting for a typo minus sign that appeared in [8]in front of the square root in the corresponding Eq. (7))

$$\sigma_{C,xy} + \left(\frac{\mu_C(\sigma_{C,xx})}{G_C}\right)\frac{d\sigma_{C,xy}}{dt} = \mu_C(\sigma_{C,xx})\dot{\gamma}, \tag{5}$$

$$\sigma_{C,xx} + \left(\frac{\mu_C(\sigma_{C,xx})}{G_C}\right)\left(\frac{d\sigma_{C,xx}}{dt} - 2\dot{\gamma}\sigma_{C,xy}\right) = 0, \tag{6}$$

where

$$\mu_C(\sigma_{C,xx}) \equiv \frac{-b + \sqrt{b^2 - 4c}}{2}. \tag{7}$$

with

$$b \equiv \tau_C\sqrt{\frac{G_C\sigma_{C,xx}}{2}} - \mu_{C0}, \text{ and} \tag{8}$$

$$c \equiv -\mu_{C\infty}\tau_C\sqrt{\frac{G_C\sigma_{C,xx}}{2}}\,. \tag{9}$$

For the last two terms in Eq. (1), we need to incorporate a thixotropic model, with a scalar thixotropic parameter, λ, to describe the amount of structure present at any time, spanning [0 1], whereby zero represents zero structure, no rouleaux, and one represents the fully structured, aggregated, blood. We follow an identical approach as Horner and coworkers, and Armstrong and Tussing with respect to capturing the elastic and viscoelastic stress contributions from the rouleaux [7-10, 42, 43, 45]. The following equation describes the evolution of the structure as a function of the shear rate of blood

$$\frac{D\lambda}{Dt} = \frac{1}{\tau_\lambda}\left(-\lambda\tau_{break}\left|\dot{\gamma}_p\right| + (1-\lambda)\left|\tau_{aggr}\dot{\gamma}_p\right|^d + (1-\lambda)\right). \tag{10}$$

Eq. (10) represents a reformulation of our previously developed structural equation [7-10, 42, 43, 45, 47, 52] using the τ_{break} and τ_{aggr} as *"material constantss"* with units of time controlling the stress-induced rouleaux breakage and stress-induced rouleaux aggregation, respectively.

As a result of the fact that both the τ_{break} and τ_{aggr} material parameters have time units, and that they both appear in Eq. (10) as a product with $\dot{\gamma}_p$ with units (s^{-1}), they can be used to define dimensionless Weissenberg numbers that control the stress-induced breakage and stress-induced aggregation rates as follows: $Wi_{break} = \tau_{break}\dot{\gamma}_p$; and $Wi_{aggr} = \tau_{aggr}\dot{\gamma}_p$. These Weissenberg numbers can then be used to define the *effective* times for stress-induced breakage and aggregation as: $\hat{\tau}_{break} = \tau_\lambda / Wi_{break}$; and $\hat{\tau}_{aggr} = \tau_\lambda / \left(Wi_{aggr}\right)^d$, effectively modifying the Brownian aggregation time

τ_λ. Thus, the τ_{break} and τ_{aggr} material parameters can be physically interpreted as defining by their inverse the characteristic shear rates for which the corresponding effective times characterizing the shear-induced breakage and aggregation, respectively, become shorter to the characteristic time τ_λ characterizing Brownian aggregation. Previous versions of the kinetic expression described in Eq. (10) used alternative forms for the kinetic parameters, most recently t_{r1} and t_{r2} [49]. Those are related to the τ_{break} and τ_{aggr} material parameters as $\tau_{break} = t_{r1}$ and $\tau_{aggr} = \left(t_{r2}\right)^{1/d}$. We prefer to use instead the τ_{break} and τ_{aggr} as they are more amenable to a physical interpretation (given above) and, given the fact that they both have time units, they can be directly compared, thus allowing for a comparison of the critical Weissenberg numbers governing both shear-induced effects (i.e. breakage and aggregation).

The right-hand-side of Eq. (10) has three terms to describe the evolution of thixotropy: 1. A shear breakdown term, proportional to shear rate and λ, proportional to the amount of structure still present; 2. A shear-rate dependent shear buildup term, proportional to a power *d* of shear rate and $(1-\lambda)$; and 3. A Brownian buildup term, proportional to $(1-\lambda)$ [7-10]. We note here that we fix d =1/2 as done in the literature for blood [7-10, 45, 47]. This kinetic expression is used here since it has been shown in the literature to model the transient dynamics of human blood rheology, specifically the breakdown and buildup of rouleaux [7-10, 45, 47].

Our thixotropic modeling incorporates kinematic hardening in the separating of strain and shear rate into elastic and plastic components following Dimitriou and coworkers [33-35] where $\gamma = \gamma_e + \gamma_p$ and $\dot{\gamma} = \dot{\gamma}_e + \dot{\gamma}_p$, with the plastic strain rate described by

$$\dot{\gamma}_p = \begin{cases} \dfrac{\dot{\gamma}}{\left(2 - \dfrac{\gamma_e}{\gamma_{\max}}\right)}, & \dot{\gamma} \geq 0 \\ \dfrac{\dot{\gamma}}{\left(2 + \dfrac{\gamma_e}{\gamma_{\max}}\right)}, & \dot{\gamma} < 0 \end{cases}, \tag{11}$$

where a subscript *e* represents the elastic component, and a subscript *p* represents the plastic component [8-10, 33, 39, 42, 43, 45]. The plastic components are involved with irreversible processes, and breakage of structure, while the elastic components are involved with reversible deformation of the rouleaux structures. In the above equation, the maximum rouleaux strain, $\gamma_{\max}$, is given as

$$\gamma_{\max} = \gamma_{0,\mathrm{R}} \lambda, \tag{12}$$

where γ_0 is the rouleaux zero-shear-strain-rate limiting elastic strain. The elastic strain rate is given as

$$\dot{\gamma}_{\mathrm{e}} = \begin{cases} \dot{\gamma}_p - \dfrac{\gamma_e}{\gamma_{max}} \left|\dot{\gamma}_p\right|, & \dfrac{D\gamma_{max}}{Dt} \geq 0 \\ \dot{\gamma}_p - \dfrac{\gamma_e}{\gamma_{max}} \left|\dot{\gamma}_p\right| + \dfrac{\gamma_e}{\gamma_{max}} \dfrac{d\gamma_{max}}{dt}, & \dfrac{D\gamma_{max}}{Dt} < 0 \end{cases}. \tag{13}$$

The steady state value of the structure parameter can then be readily calculated as

$$\lambda_{ss} = \frac{\left(\left|\tau_{\mathrm{aggr}} \dot{\gamma}\right|^d + 1\right)}{\left(\tau_{\mathrm{break}} \left|\dot{\gamma}\right| + \left|\tau_{\mathrm{aggr}} \dot{\gamma}\right|^d + 1\right)}. \tag{14}$$

The steady state value of the structure parameter must lie between zero and one, whereby a value of zero signifies no 'bonds' with nearest neighbor red blood cells, and a value of one represents maximum

number of structure formation with respect to rouleaux formation. It is understood that the breakdown and buildup of microstructure (rouleaux of human blood) is analogous to a reversible chemical reaction that is in a state of dynamic equilibrium at constant pressure and temperature, where the equilibrium concentrations of reactive species are constant, however some reactant molecules are still reacting to form products, and some product molecules are reacting to form reactants. The only stipulation at chemical equilibrium is that the concentrations are constant. For human blood rouleaux the average amount of microstructure is constant at each constant shear rate. However, like the reversible chemical reaction at equilibrium, some of the rouleaux are broken down (forward process), while some of the red blood cells are forming rouleaux (reverse process). The only requirement for our argument is the 'mean' structure level at any given constant shearing strain-rate must stay constant, thereby making the overall time derivative of the structure zero.

The elastic contribution from rouleaux to total shear stress is then calculated as

$$\sigma_{E,xy} = \frac{\sigma_{y,0}}{\gamma_{0,R}}\gamma_e, \tag{15}$$

where $\sigma_{y,0}$ is the yield-stress. In turn, in the ETV model, the viscoelastic contribution to total shear stress from rouleaux is specified as obeying the following evolution equation

$$\frac{D}{Dt}\sigma_{V,xy} = \begin{cases} G_R\lambda^m\left(\dot{\gamma} - \frac{\sigma_{V,xy}}{\mu_R\lambda^m}\right), & \dot{\lambda} \geq 0 \\ G_R\lambda^m\left(\dot{\gamma} - \frac{\sigma_{V,xy}}{\mu_R\lambda^m}\right) + m\frac{\sigma_{V,xy}}{\lambda}\dot{\lambda}, & \dot{\lambda} < 0 \end{cases}, \tag{16}$$

where $\dot{\lambda} = D\lambda/Dt$. Note that in this equation we introduce the only difference between the ETV and the previous ethixo-mHAWB model by replacing the $\dot{\gamma}_p$ term with $\dot{\gamma}$.

II.2 ESSTV MODEL

The Enhanced Structural Stress Thixotropic Viscoelastic (ESSTV) model was developed as a modification of the ETV model following a novel viscoelastic-elastic formulation using recently published theories of plasticity [31, 37] that allow to express both the elastic and viscoelastic stress contributions of blood rouleaux microstructures in one state of total elastoviscoplastic stress. Therefore, in this model, the total shear stress, σ_{xy}, involves only two contributions, the viscoelastic free cell contribution, $\sigma_{C,xy}$, and the new single elastoviscoplastic rouleaux contribution, $\sigma_{R,xy}$, thus, replacing Eq. (1) with

$$\sigma_{xy} = \sigma_{C,xy} + \sigma_{R,xy}. \tag{17}$$

In the above equation the viscoelastic contribution of the deformed RBCs, $\sigma_{C,xy}$, is defined exactly as in the ETV model, i.e., through Eqs. (5-7). In addition, the time evolution governing the structural parameter λ remains the same, Eq. (10) as well as the governing equations for the elastic component of the strain and strain rate, Eqs. (11-13) thereby resulting to the same expression for the steady state value of the structural parameter λ, Eq. (14) .

The proposed combined elastoviscoplastic rouleaux contribution (following the motivation from Saramito [31], Wei et al. [36], and Varchanis et al. [37]) from the rouleaux to the total stress for the ESSTV model is defined by

$$\frac{1}{G_R\lambda}\frac{D}{Dt}\sigma_{R,xy} + \max\left(0, \frac{\left|\sigma_{R,xy} - \left(\frac{\sigma_{y,0}}{\gamma_{0,R}}\right)\left|\gamma_e\right|\right|}{\mu_R\lambda^m\left|\sigma_{R,xy}\right|}\right)\sigma_{R,xy} = \dot{\gamma}, \tag{18}$$

where G_R is the elastic modulus of the rouleaux, μ_R is the rouleaux structural viscosity, and m is a fitting parameter, here set to *3/2* [7-9, 10, 41, 43]. Again, the right-hand side of Eq. (18) is the total shear rate. Eq. (18) is inspired by Varchanis et al. and Wei et al. [36, 37] designating the evolution of the total, elastic plus viscoelastic, contribution from the rouleaux to the stress. An alternative, mathematically equivalent, reformulation of Eq. (18) that has advantages from a computational viewpoint is

$$\frac{1}{G_R\lambda}\frac{D}{Dt}\sigma_{R,xy}+\max\left(0,\frac{\left|\sigma_{R,xy}-\left(\frac{\sigma_{y,0}}{\gamma_{0,R}}\right)|\gamma_e|\right|}{\mu_R\lambda^m}\right)\text{sign}(\sigma_{R,xy})=\dot{\gamma}\,. \tag{19}$$

Note that the steady state value of the shear stress is the same for both ETV and ESSTV models

$$\sigma_{ss}=\eta_C(\dot{\gamma})\dot{\gamma}+\mu_R\lambda_{ss}^m\dot{\gamma}+\sigma_{y,0}\lambda_{ss}\,. \tag{20}$$

Table I below contains the complete set of equations for the two models communicated here, ETV and ESSTV.

Table I. Summary and comparison of the ETV and ESSTV models

Model	ETV	ESSTV
PAR.	$\mu_0, \mu_\infty, \mu_R, \tau_c, \sigma_{y0}, \tau_{break}, \tau_{aggr}, \gamma_{0,R}, d, m, G_c, G_R, \tau_\lambda$	
SS	$\sigma_{ss} = \sigma_{ve,ss} + \mu_R \lambda_{ss}^m \dot{\gamma} + \sigma_{y,0} \lambda_{ss}$ $\sigma_{ve,ss} = \left(\mu_\infty + \frac{(\mu_0 - \mu_\infty)}{(1+\tau_C \dot{\gamma})} \right) \dot{\gamma}$	$\lambda_{ss} = \frac{\left(\lvert \tau_{aggr} \dot{\gamma} \rvert^d + 1 \right)}{\left(\tau_{break} \lvert \dot{\gamma} \rvert + \lvert \tau_{aggr} \dot{\gamma} \rvert^d + 1 \right)}$
VE, plasma	$\dot{\gamma}_p = \begin{cases} \frac{\dot{\gamma}}{\left(2 - \frac{\gamma_e}{\gamma_{max}}\right)}, & \dot{\gamma} \geq 0 \\ \frac{\dot{\gamma}}{\left(2 + \frac{\gamma_e}{\gamma_{max}}\right)}, & \dot{\gamma} < 0 \end{cases}$ $\gamma_{max} = \gamma_{0,R} \lambda$ $\sigma_{yx,ve} + \left(\frac{\eta_c(\sigma_{xx,ve})}{G_c} \right) \frac{d\sigma_{yx,ve}}{dt} = \eta_c(\sigma_{xx,ve}) \dot{\gamma}$ $\sigma_{xx,ve} + \left(\frac{\eta_c(\sigma_{xx,ve})}{G_c} \right) \left(\frac{d\sigma_{xx,ve}}{dt} - 2\dot{\gamma}\sigma_{yx,ve} \right) = 0$	$\frac{D\lambda}{Dt} = \frac{1}{\tau_\lambda} \left(-\lambda \tau_{break} \lvert \dot{\gamma}_p \rvert + (1-\lambda) \lvert \tau_{aggr} \dot{\gamma}_p \rvert^d + (1-\lambda) \right)$ $\dot{\gamma}_e = \begin{cases} \dot{\gamma}_p - \frac{\gamma_e}{\gamma_{max}} \lvert \dot{\gamma}_p \rvert, & \frac{d\gamma_{max}}{dt} \geq 0 \\ \dot{\gamma}_p - \frac{\gamma_e}{\gamma_{max}} \lvert \dot{\gamma}_p \rvert + \frac{\gamma_e}{\gamma_{max}} \frac{d\gamma_{max}}{dt}, & \frac{d\gamma_{max}}{dt} < 0 \end{cases}$ $b = \tau_c \sqrt{\frac{G_c \sigma_{xx,ve}}{2}} - \mu_0 \qquad c = -\mu_{\infty,c} \tau_c \sqrt{\frac{G_c \sigma_{xx,ve}}{2}}$ $\eta_c(\sigma_{xx,ve}) = \frac{-b + \sqrt{b^2 - 4c}}{2}$
VE, rouleaux	$\frac{d\sigma_{yx,R,ve}}{dt} = \begin{cases} G_R \lambda^m \left(\dot{\gamma} - \frac{\sigma_{yx,r,ve}}{\mu_R \lambda^m} \right), & \frac{d\lambda}{dt} \geq 0 \\ G_R \lambda^m \left(\dot{\gamma} - \frac{\sigma_{yx,r,ve}}{\mu_R \lambda^m} \right) + m \frac{\sigma_{yx,R,ve}}{\lambda} \frac{d\lambda}{dt}, & \frac{d\lambda}{dt} < 0 \end{cases}$ $\sigma_{yx,R,e} = \frac{\sigma_{y,0}}{\gamma_{0,R}} \gamma_e$	$\frac{1}{\lambda G_R} \dot{\sigma}_{yx,R,evp} + \max \left(0, \frac{\left\lvert \sigma_{yx,R,evp} - \left(\frac{\sigma_{y0}}{\gamma_{0,R}} \right) \gamma_e \right\rvert}{(\lambda^m \mu_R) \lvert \sigma_{yx,R,evp} \rvert} \right) \sigma_{yx,R,evp} = \dot{\gamma}$
Transient	$\sigma_{trans} = \sigma_{yx,ve} + \sigma_{yx,R,ve} + \sigma_{yx,R,e}$	$\sigma_{trans} = \sigma_{yx,ve} + \sigma_{yx,R,evp}$

II.3 t-ETV and t-ESSTV Models

The tensorial version of both ETV and ESSTV models follow Wei et al, Varchanis et al. and Armstrong et al., [36,37,45,47] by exchanging the material time derivative, $D/Dt\, \sigma_{V,xy}$, in Eqs. (16) and (18) with their upper-convected time equivalents, $\overset{\nabla}{\sigma}_{V,xy}$ or $\overset{\nabla}{\sigma}_{R,xy}$. This by necessity generates a coupling of the shear to the other components of the stress, most notably the normal ones. The mathematical structure enters through the coupling of terms among various terms of the two tensors and their time derivatives. The resulting equations for the *xy*, *xx*, *yy*, and *zz* components

are shown in Table II, below. We acknowledge that one may choose to use different criteria for yielding in the numerator of the conditional. As an example, the Von Mises yield criteria: $\left|\sqrt{3}\sigma_{xy}\right| - \lambda\sigma_{xy}$ [36, 37, 43, 45, 50]. The tensorial models here are applicable to shear flow, and the shear rate, $\dot{\gamma}$ is replaced as follows [25, 37. 47]. Here, we follow the work of Wei et al. [36], where $\tilde{\sigma}=\sqrt{\frac{\underline{\underline{\sigma}}_R^D:\underline{\underline{\sigma}}_R^D}{2}}$, and $\underline{\underline{\sigma}}_R^D=\underline{\underline{\sigma}}_R-\frac{\mathrm{tr}(\underline{\underline{\sigma}}_R)}{3}\underline{\underline{I}}$. Where $\tilde{\sigma}$ is the equivalent shear stress, "*D*" means deviatoric part of the tensor, $\underline{\underline{I}}$ is the unit tensor, '*:*' is the double dot product, and the trace is $\mathrm{tr}(\underline{\underline{\sigma}}_R)=(\sigma_{R,xx}+\sigma_{R,yy}+\sigma_{R,zz})$.

$$\underline{\underline{\gamma}}_{(1)}=\dot{\gamma}_{ij}=\nabla v+(\nabla v)^T=\begin{pmatrix}0&1&0\\1&0&0\\0&0&0\end{pmatrix}\dot{\gamma}_{yx}. \tag{21}$$

Table II. Summary and comparison of the t-ETV and t-ESSTV stress components of the rouleaux viscoelastic and elastoviscoplastic, respectively, contributions to total stress [36, 37, 43].

Model	t-ETV	t-ESSTV
xx	$\frac{d\sigma_{R,xx}}{dt} - 2\sigma_{R,yx}\dot{\gamma} = \begin{cases} G_R\lambda^m\left(-\frac{\sigma_{R,xx}}{\mu_R\lambda^m}\right), & \frac{d\lambda}{dt} \geq 0 \\ G_R\lambda^m\left(-\frac{\sigma_{R,xx}}{\mu_R\lambda}\right) + m\frac{\sigma_{R,xx}}{\lambda}\frac{d\lambda}{dt}, & \frac{d\lambda}{dt} < 0 \end{cases}$	$\frac{1}{\lambda G_R}\left(\frac{d\sigma_{R,xx}}{dt} - 2\sigma_{R,yx}\dot{\gamma}\right) + \max\left(0, \frac{\left\lvert\tilde{\sigma} - \left(\frac{\sigma_{y0}}{\gamma_{0,R}}\right)\lvert\gamma_e\rvert\right\rvert}{(\lambda^m\mu_R)\tilde{\sigma}}\right)\sigma_{R,xx} = 0$
yy	$\frac{d\sigma_{R,yy}}{dt} = \begin{cases} G_R\lambda^m\left(-\frac{\sigma_{R,yy}}{\mu_R\lambda^m}\right), & \frac{d\lambda}{dt} \geq 0 \\ G_R\lambda^m\left(-\frac{\sigma_{R,yy}}{\mu_R\lambda^m}\right) + m\frac{\sigma_{R,yy}}{\lambda}\frac{d\lambda}{dt}, & \frac{d\lambda}{dt} < 0 \end{cases}$	$\frac{1}{\lambda G_R}\frac{d\sigma_{R,yy}}{dt} + \max\left(0, \frac{\left\lvert\tilde{\sigma} - \left(\frac{\sigma_{y0}}{\gamma_{0,R}}\right)\lvert\gamma_e\rvert\right\rvert}{(\lambda^m\mu_R)\tilde{\sigma}}\right)\sigma_{R,yy} = 0$
zz	$\frac{d\sigma_{R,zz}}{dt} = \begin{cases} G_R\lambda^m\left(-\frac{\sigma_{R,zz}}{\mu_R\lambda^m}\right), & \frac{d\lambda}{dt} \geq 0 \\ G_R\lambda^m\left(-\frac{\sigma_{R,zz}}{\mu_R\lambda^m}\right) + m\frac{\sigma_{R,zz}}{\lambda}\frac{d\lambda}{dt}, & \frac{d\lambda}{dt} < 0 \end{cases}$	$\frac{1}{\lambda G_R}\frac{d\sigma_{R,zz}}{dt} + \max\left(0, \frac{\left\lvert\tilde{\sigma} - \left(\frac{\sigma_{y0}}{\gamma_{0,R}}\right)\lvert\gamma_e\rvert\right\rvert}{(\lambda^m\mu_R)\tilde{\sigma}}\right)\sigma_{R,zz} = 0$
yx	$\frac{d\sigma_{R,yx}}{dt} - \sigma_{R,yy}\dot{\gamma} = \begin{cases} G_R\lambda^m\left(\dot{\gamma} - \frac{\sigma_{R,yx}}{\mu_R\lambda^m}\right), & \frac{d\lambda}{dt} \geq 0 \\ G_R\lambda^m\left(\dot{\gamma} - \frac{\sigma_{R,yx}}{\mu_R\lambda^m}\right) + m\frac{\sigma_{R,yx}}{\lambda}\frac{d\lambda}{dt}, & \frac{d\lambda}{dt} < 0 \end{cases}$	$\frac{1}{\lambda G_R}\left(\frac{d\sigma_{R,yx}}{dt} - \sigma_{R,yy}\dot{\gamma}\right) + \max\left(0, \frac{\left\lvert\tilde{\sigma} - \left(\frac{\sigma_{y0}}{\gamma_{0,R}}\right)\lvert\gamma_e\rvert\right\rvert}{(\lambda^m\mu_R)\tilde{\sigma}}\right)\sigma_{R,yx} = \dot{\gamma}$

The t-ETV model is convenient to have, as straightforward manipulations show that the viscoelastic stress tensor contribution of the rouleaux structures, $\boldsymbol{\sigma}_V$, can equivalently be represented in terms of a conformation tensor $\mathbf{c}_V$ as

$$\boldsymbol{\sigma}_V = G_R\lambda^m\left(\mathbf{c}_V - \boldsymbol{\delta}\right), \tag{22}$$

with the conformation tensor $\mathbf{c}_V$ obeying the following time evolution equation

$$\overset{\triangledown}{\mathbf{c}}_V = -\left(\frac{G_R\lambda^m}{\mu_R} + \frac{m}{2\lambda}\left(\frac{d\lambda}{dt} + \left|\frac{d\lambda}{dt}\right|\right)\right)\left(\mathbf{c}_V - \boldsymbol{\delta}\right). \tag{23}$$

This is fully compatible to nonequilibrium thermodynamics, obeying all entropy related constraints, corresponding to a simple Hookean dumbbell with $G_R\lambda^m$ as modulus, and a characteristic relaxation time τ_R dependent on both λ and $d\lambda/dt$ defined as

$$\tau_R \equiv \frac{1}{\left(\frac{G_R \lambda^m}{\mu_R} + \frac{m}{2\lambda}\left(\frac{d\lambda}{dt} + \left|\frac{d\lambda}{dt}\right|\right)\right)} \ . \tag{24}$$

Note that no matter what the sign of $d\lambda/dt$ is, τ_R is always positive, thus ensuring that the proper thermodynamic constraints are satisfied [26].

III. EXPERIMENTAL METHODS

A. Materials and sample preparation

The handling and rheological measurement protocol employed for the blood rheology in this work follow previous established guidelines for blood rheology, and directly follows the protocol described by Horner and coworkers here [7, 8, 9, 39]. A complete and detailed description of the blood draw procedure can be found here [8, 9, 39]. "For rheological experiments 6mL of blood was drawn into a vacutainer tube with 1.8 mg/mL of EDTA. An additional 9 mL of blood was drawn and sent for a Complete Blood Count, Lipid Panel and Fibrinogen Activity test" [7,14,40]. Results are shown in Table III [8, 9, 39].

Table III: Physiological parameter values of five donors [52-57].

Donor	Hematocrit (%)	Fibrinogen (mg/dL)	Total Cholesterol (mg/mL)	Triglycerides (mg/mL)	HDL Cholesterol (mg/mL)	LDL Cholesterol (mg/mL)
1	43.6	0.252	174	58	59	101
2	43.4	0.248	147	40	51	85
3	42.2	0.246	148	29	56	85
4	43.8	0.199	197	82	78	102
5	45.1	0.21	204	102	71	113

The rheological data were collected with an ARESG2 strain-controlled rheometer from TA Instruments using a double wall Couette [8, 9, 39]. The dimensions and measurable range can be found here [7,14,40]. All rheological tests were performed at 37^{o}C, maintained by a Peltier temperature controller. The shear rate did not exceed 1000s^{-1} and a preshear of 300s^{-1} for 30s was incorporated before each rheological test to eliminate thixotropic, or memory effects [8, 9, 39]. Experimental results will be shown for steady state, step up/down in shear rate tests, small amplitude oscillatory shear, SAOS, amplitude sweep at $\omega = 10(\text{rad}/\text{s})$, large amplitude oscillatory shear (LAOS) and uni-directional large amplitude oscillatory shear flow (UD-LAOS) [7, 8, 9, 48, 49]. These experimental procedures and protocols follow exactly the work of Horner and coworkers [8, 9, 39], and all the rheological data for the five donors in Table III can be found on Mendeley Data [52-55]. The LAOS and UD-LAOS experiments presented in this work follow the same protocol as described by Horner and coworkers [8, 9, 48, 49] and Armstrong and coworkers [41, 43] where the shear strain and shear strain rates are defined as

$$\gamma(t) = \gamma_0 \sin(\omega t), \quad \text{and} \tag{25}$$

$$\dot{\gamma}(t) = \gamma_0 \omega \cos(\omega t), \tag{26}$$

for the LAOS experiments and

$$\gamma(t) = \gamma_0 \sin(\omega t) + t\gamma_0\omega \ , \tag{27}$$

$$\dot{\gamma}(t) = \gamma_0\omega\cos(\omega t) + \gamma_0\omega \tag{28}$$

for the UD-LAOS [8, 9, 41, 43, 51]. The UD-LAOS data and model fits are plotted using effective Lissajous-Bowditch elastic and viscous projections, where the measured stress is a function of the oscillatory component of the strain and shear rate as shown in Eqs. (25) and (26) respectively [8, 9, 41, 43].

The small amplitude oscillatory shear (SAOS) follows the standard formalism

$$\tau_{yx}(t) = \gamma_0 \sum_{i,odd}^{n} \left(G_i^{'} \sin(n\omega t) + G_i^{"} \cos(n\omega t) \right). \tag{29}$$

Where $n=1$, for SAOS. We note here that Eq. (29) is a function of time t, frequency ω, and strain amplitude γ_0. In addition, it is noted that for LAOS n is the running index (when not equal to one), and the upper limit of the summation goes to infinity. We use the ratio of third to first harmonic as a metric of success of our model predictions as

$$\frac{I_3}{I_1} = \sqrt{\frac{(G_3^{'2} + G_3^{"2})}{(G_1^{'2} + G_1^{"2})}} \ , \tag{30}$$

where the subscript *3* are the third harmonic values [8, 9, 41, 43]. Eq. (30) is the relative intensity of the third harmonic normalized by the first harmonic intensity and will be used as a metric of model efficacy, and shown on the SAOS predictions for each model in Figs. 2, 4, 6 and 8 below [8, 9, 41, 43].

B. Parameter optimization

For the model fitting procedure, we follow the previous protocol as established by Horner and coworkers with the following modifications [7-9, 41, 43 ,46-48]. 1. The steady state parameters are fit to steady state data by minimizing the *normalized* cost function, $F_{cost,ss}$, then held constant for a preliminary run, to obtain an initial guess. The initial guess of the steady state parameters are found using a parallel tempering algorithm, and Eq. 31 shown below [8, 9, 41, 43]

$$F_{cost,ss} = \frac{1}{N}\sqrt{\sum_{i=1}^{N}\left(\frac{(y_i - f_i)}{y_i}\right)^2}, \tag{31}$$

where y_i is the steady state stress data and f_i is the model prediction; 2. The initial guesses from part one are incorporated as a starting point, and then *all* parameters are simultaneously fitted as part of the tempering algorithm (and non-dimensionalized as per Eq. 32). The transient three step-ups in shear rate and three step-downs in shear rate are non-dimensionalized with the maximum stress values from each of the respective step change in shear rate experiments. This normalization scheme was selected due to the relative equivalent order of magnitude of the maximum stress values over all the step-up/downs, to maintain an even, unbiased fitting of parameters with minimum bias towards any one of the step experiments. The transient parameters to *three* sets of step-ups in shear rate and *three* sets of step-downs in shear rate experiments, again with parallel tempering, minimizing the following cost function

$$F_{cost,tot} = \frac{1}{N}\sqrt{\sum_{j=1}^{N}\left(\frac{(y_j - f_j)}{y_j}\right)^2} + \frac{1}{M}\sum_{k=1}^{M}\frac{1}{K}\sqrt{\sum_{i=1}^{K}\left(\frac{(y_i - f_i)}{y_{K,max}}\right)^2} \tag{32}$$

where N is the total number of steady state data points, M is the total number of transient step up/down in shear rate tests and K is the number of points per transient experiment [8, 9, 41, 43]. The model is fit directly to rheology data using the Matlab *ode23s* function to integrate the

differential equations [8, 9, 41, 43]. When fitting all the parameters together, $F_{cost,tot}$ must be non-dimensionalized to provide a balanced fit. A Dell laptop with 8GB RAM was used for computation of the parameters using parallel tempering. Although ode45 is considered more accurate, it struggles with stiff odes. Ode23s can solve stiff systems of odes, while simultaneously maintaining enough accuracy to provide robust fits with all the models tested here [8, 9, 41, 43]. With the parameters fit, they are kept *constant* to predict a series of: SAOS (amplitude sweep), 17 sets of LAOS at frequencies 0.5, 1, and 5 (rad/s), at strain amplitudes of 0.5, 1.0, 5.0, 10.0, 50.0 and 100 (-); and six sets of UD-LAOS experiments at a frequency of 1 (rad/s) and strain amplitudes of 1.0, 5.0, 10 and 50 (-). The predictions for each are shown in Figs. 9 and 10 below, with cost functions computed for each set of LAOS and UD-LAOS as

$$F_{cost,LAOS} = \frac{1}{N}\sqrt{\sum_{i=1}^{N}\left(y_i - f_i\right)^2}\,. \tag{33}$$

The small amplitude oscillatory shear is predicted, and $F_{cost,SAOS}$ computed as follows

$$F_{cost,SAOS} = \sum_{i=1}^{n}\left(\sqrt{\left(G'_{i,data} - G'_{i,model}\right)^2} + \sqrt{\left(G''_{i,data} - G''_{i,model}\right)^2}\right)/(2n)\,, \tag{34}$$

where n is the number of points. $F_{cost,SAOS}$ is calculated for the amplitude sweep. The fit model parameters are held constant, and used to predict a full period at alternance, and using the $\boldsymbol{A}=\boldsymbol{b}x$ where $\boldsymbol{A}$ is an array consisting of two columns: $\gamma_0 sin(\omega t)$ and $\gamma_0 cos(\omega t)$ and $\boldsymbol{b}$ is the stress prediction over a period. Using the $x=\boldsymbol{A}\backslash\boldsymbol{b}$ command in Matlab the first harmonic moduli (G_1' and G_1'') are calculated and compared to the data at each combination of strain amplitude and frequency in both sets of SAOS, amplitude and frequency sweeps. In addition, the third harmonic moduli are calculated (G_3' and G_3'') to compare with the data, and shown in Fig. 2, 4, 6 and 8 below [41, 43]. A summation of the cost functions of the step-ups/downs (fits), SAOS,

LAOS and UDLAOS predictions is then used to assess overall model efficacy (shown in Table VII). This concludes our discussion of F_{cost} for the SAOS predictions.

Each of the LAOS and UD-LAOS predictions accumulate $F_{cost,LAOS}$ over three periods of data, with the Lissajous-Bowditch elastic and viscous projections showing the last period data and predictions. The full set of best fit parameters for Donors 1-5 are shown in Tables IV-VII below) There is a modified procedure for fitting the full tensorial version of both the ETV and ESSTV models. The modification is as follows: 1. The initial parameter guess is provided from the best fit values of the non-tensorial versions respectively; and 2. The steady state and transient parameters are fit simultaneously with the steady state cost function accumulated without normalization with the stress measurement at each point.

IV.RESULTS AND DISCUSSION

A. ETV model

The ETV has a total of ten parameters that are simultaneously fit to steady state, and the transient step up/down in shear rate experiments, after a preliminary run with the steady state to obtain an initial guess. Ten parameters (color coded yellow in Table IV) of the parameters are fit to steady state and step-up/downs; with three fixed as follows: $\gamma_{0,R}$ set to one, as recommended as best fit value from literature [7-9, 41, 43]; with m set to 3/2; and d set to ½. For a total of 13 parameters (including the three fixed parameters, seven preliminarily fit to steady state data, and all parameters fit to steady state and transient data together). Table IV provides a synopsis of all the model parameters for convenience [9, 10].

Table IV: Model parameter description and units of the ETV, ESSTV, t-ETV and t-ESSTV models [9,10]

Parameter	Units	Description
$\mu_{0,c}$	Pa s	zero sher viscosity of plasma and suspended RBCs
$\mu_{\infty,c}$	Pa s	infinite shear viscosity of plasma and suepended RBCs
τ_C	s	RBC deformation time constant (Cross constant)
τ_{break}	s	material constant for stress-induced breakdown
τ_{aggr}	s	material constant for stress-induced aggregation
μ_R	Pa s	rouleaux viscosity
σ_{y0}	Pa	yield stress
γ_0	(-)	rouleaux zero shear rate limiting elastic strain
d	(-)	power law of shear buildup from shear
m	(-)	rouleaux power law constant
τ_λ	s	overal rouleaux rebuild time constant
G_R	Pa	rouleaux elastic modulus
G_C	Pa	RBCs elastic modulus

Fig. 1(a) shows the steady state fit, and Fig. 1(b) and (d) show the fit to the three step-downs and three step-ups in shear rate, respectively. Recall that a good initial guess is first obtained for the steady state parameters, then using these values as a starting point, all the parameters are then fit simultaneously to the steady state data and the set of six step ups/downs in shear rate transient experiments. Fig. 1(c) and (e) are showing the corresponding evolution of the structure parameter during the step down and step up in shear rate experiments. From Fig. 1(b) it is apparent that the model can capture the changing stress during the step-up and step-down experiments. Table V shows the best fit model parameters from the steady state and transient data fit, and the value of F_{cost} for the steady state and step up/downs for Donor 3. Additionally, the dimensional F_{cost} of the SAOS prediction is shown in Table V. (Donor 1-5 best fit parameter values are shown in Table V; the F_{cost} for SAOS, LAOS and UDLAOS predictions is shown for Donor 3 in Table IX). We again note here that the steady state $F_{cost,tot}$ is dimensionless because the difference between the model and data was normalized with the value of each data point for

steady state, and the maximum stress value from the data over each respective transient for the step up/downs. Fig. 2 shows the model *predictions* to the SAOS amplitude sweep.

FIG. 1 ETV model fit for (a) steady state human blood data; (b) set of 3 step-up in shear rate from $\dot{\gamma}$ of $0.1s^{-1}$ to 5, 10, and $20s^{-1}$; (c) corresponding structure parameter curves (colors of structure parameter curves match respective colors from stress evolution curves); (d) step-down in shear rate to $\dot{\gamma}$of $0.1s^{-1}$ from 5, 10, and $20s^{-1}$; and (e) corresponding structure parameter curves (Donor3) (dataset3) [55].

FIG. 2 Small amplitude oscillatory shear, amplitude sweep performed at $\omega = 12.6(\mathrm{rad/s})$, data discrete point, and predictions, dashed lines of ETV(Donor3) (dataset3) [55].

Table V: Best fit parameter values of ETV model for Donors 1-5 [52-57] (F_{cost} steady state and step-up/downs dimensionless; $F_{cost,SAOS}$ has units of (Pa)).

ETV (Non-tensorial)								
	Par.	**Donor1**	**Donor2**	**Donor3**	**Donor4**	**Donor5**	**Ave.**	**Stdev**
SS	$\mu_{0,c}$ **(Pa s)**	0.0081	0.0080	0.0079	0.0074	0.0101	0.0083	0.0010
	$\mu_{\infty,c}$ **(Pa s)**	0.0033	0.0033	0.0032	0.0035	0.0037	0.0034	0.0002
	τ_C **(s)**	0.049	0.050	0.030	0.043	0.065	0.0474	0.0127
	τ_{break} **(s)**	0.874	0.872	1.146	1.087	0.966	0.9888	0.1243
	τ_{aggr} **(s)**	6.36E-04	6.41E-04	4.24E-02	1.61E-02	1.51E-05	1.20E-02	1.83E-02
	μ_R **(Pa s)**	0.033	0.033	0.032	0.047	0.045	0.0381	0.0072
	σ_{y0} **(Pa)**	0.0021	0.0025	0.0039	0.0022	0.0022	0.0026	0.0007
	γ_0 **(-)**	1	1	1	1	1	-	-
	d (-)	1/2	1/2	1/2	1/2	1/2	-	-
	m (-)	3/2	3/2	3/2	3/2	3/2	-	-
	F_{cost} **(SS)***	**0.0077**	**0.0117**	**0.0102**	**0.0056**	**0.0091**	**0.0088**	**0.0023**
trans, ETV	τ_λ **(s)**	1.8051	1.7645	1.9106	2.7877	2.1465	2.0829	0.4210
	G_R**(Pa)**	0.1494	0.1532	0.2671	0.1593	0.1446	0.1747	0.0519
	G_c **(Pa)**	0.3526	0.3421	0.4703	0.3281	0.6197	0.4226	0.1239
	F_{cost} **(trans)***	**0.0187**	**0.0220**	**0.0204**	**0.0187**	**0.0208**	**0.02012**	**0.0014**
	Fcost (SAOS)	**0.0022**	**0.0024**	**0.0034**	**0.0016**	**0.0019**	**0.00231**	**0.0007**

B. ESSTV

The enhanced structural stress-ETV or ESSTV, has the same number of parameters as the ETV, with a total of seven parameters fit to steady state, to obtain an initial guess, and then all ten

parameters are fit simultaneously to the steady state and three more fit to the transient step up/down in shear rate experiments. Ten parameters (color coded green in Table V) of the parameters are fit to steady state and transient ; with three fixed as follows: $\gamma_{0,R}$ set to one, as recommended as best fit value from literature [7-9, 41, 43]; with m set to 3/2; and d set to ½. For a total of 13 parameters (including the three fixed parameters, seven fit to steady state data first to obtain a good to obtain an initial guess, and then all ten are fit to steady state and transient simultaneously). Fig. 3(a) shows the steady state fit, and Fig. 3(b) and (d) show the fit to the three step-down and three step-ups in shear rate, respectively. Recall that the steady state parameters are fit first to the steady state to obtain an initial guess, and then all the parameters fit to steady state and the set of six step up/down in shear rate transient experiments. Fig. 3(c) and (e) are showing the corresponding evolution of the structure parameter during the step down and step up in shear rate experiments. From Fig. 3(b) it is apparent that the model can capture the changing stress during the step-down experiments. Table VI shows the best fit model parameters from the steady state and transient data fit, and the value of F_{cost} for the steady state, step up/downs and dimensional F_{cost} for the SAOS predictions for Donor 1-5. (Donor 1-5 best fit parameter values are shown in Table VI; the F_{cost} for all predictions together, with aggregated best values: SAOS; LAOS; and UDLAOS; is shown for Donor 3 in Table IX; and all Donors 1-5 average comparisons in Table X). We again note here that the steady state and the transient F_{cost} is dimensionless because the difference between the model and data was normalized with the value of each data point for steady state, and maximum transient stress value for the step up/down in shear rate tests. Fig. 4 shows the model predictions to the SAOS amplitude sweep. LAOS and UDLAOS predictions are shown below in the model comparison section. Comparison of Figs. 1(b) and (d) to Figs. 3(b) and (d) show that both versions of the model have approximately the same value for $F_{cost,transient}$, with ESSTV

showing a slight advantage in predicting the amplitude sweep accurately for Donor 3. Similar average trends are observed in Table X.

FIG. 3 ESSTV model fit for (a) steady state human blood data; (b) set of 3 step-up in shear rate from $\dot{\gamma}$ of $0.1s^{-1}$ to 5, 10, and $20s^{-1}$; (c) corresponding structure parameter curves (colors of structure parameter curves match respective colors from stress evolution curves); (d) step-down in shear rate to $\dot{\gamma}$ of $0.1s^{-1}$ from 5, 10, and $20s^{-1}$; and (e) corresponding structure parameter curves (Donor3) (dataset3) [55].

FIG. 4 Small amplitude oscillatory shear, amplitude sweep performed at $\omega = 12.6(\text{rad}/\text{s})$, data discrete point, and predictions, dashed lines of ESSTV (Donor3) (dataset3) [55].

Table VI: Best fit parameter values of ESSTV model for Donors 1-5 [52-57] (F_{cost} steady state and step-up/downs dimensionless; $F_{cost,SAOS}$ has units of (Pa)).

ESSTV (Non-tensorial)								
	Par.	**Donor1**	**Donor2**	**Donor3**	**Donor4**	**Donor5**	**Ave.**	**Stdev**
SS	$\mu_{0,c}$ **(Pa s)**	0.0080	0.0066	0.0079	0.0079	0.0099	0.0081	0.001199
	$\mu_{\infty,c}$ **(Pa s)**	0.0033	0.0032	0.0032	0.0035	0.0038	0.0034	0.0002
	τ_C **(s)**	0.050	0.029	0.030	0.044	0.066	0.0436	0.0151
	τ_{break} **(s)**	0.872	1.141	1.148	1.083	0.972	1.0433	0.1189
	τ_{aggr} **(s)**	6.14E-04	4.26E-02	4.35E-02	1.63E-02	1.79E-05	2.06E-02	2.15E-02
	μ_R **(Pa s)**	0.034	0.036	0.033	0.033	0.044	0.0360	0.0047
	σ_{y0} **(Pa)**	0.002	0.003	0.003	0.002	0.003	0.0026	0.0005
	$\gamma_{0,R}$ **(-)**	1	1	1	1	1	-	-
	d (-)	1/2	1/2	1/2	1/2	1/2	-	-
	m (-)	3/2	3/2	3/2	3/2	3/2	-	-
	F_{cost} **(SS)***	**0.0081**	**0.0062**	**0.0135**	**0.0072**	**0.0069**	**0.0084**	**0.002941**
trans, ESSTV	τ_λ **(s)**	0.9188	1.1358	1.3735	1.1159	1.1980	1.1484	0.1636
	G_R**(Pa)**	0.1053	0.1248	0.1364	0.1147	0.1023	0.1167	0.0141
	G_c **(Pa)**	0.5338	0.4702	0.5787	0.6272	0.6021	0.5624	0.0620
	F_{cost} **(trans)***	**0.0155**	**0.0180**	**0.0214**	**0.0113**	**0.0122**	**0.0157**	**0.0042**
	Fcost (SAOS)	**0.0016**	**0.0016**	**0.0018**	**0.0013**	**0.0016**	**0.0016**	**0.0002**

C. t-ETV

The t-ETV full tensor has the same number of parameters as the ETV, with a total of thirteen parameters fit simultaneously to steady state and six steps up/down in shear rate

experiments. As before three of the thirteen parameters are then fixed: $\gamma_{0,R}$ set to one, as a recommended value from literature [7-9, 36, 37, 42, 43]; while *d* and *m* remain 1/2 and 3/2 respectively. Fig. 5(a) shows the steady state fit, and Fig. 5(b) and (d) show the fit to the three step-down and three step-ups in shear rate, respectively. Fig. 5(c) and (e) are showing the corresponding evolution of the structure parameter during the step down and step up in shear rate experiments. Table VII shows the best fit model parameters from the simultaneous steady state and transient data fit using the t-ETV model, and the value of $F_{cost,ss}$ for the steady state, step up/downs for Donor 3 (Donor 1-5 parameter values are shown in Table VII; the F_{cost} for SAOS, LAOS and UDLAOS predictions is shown for Donor 3 in Table IX). It is important to mention that due to the tensorial format of the equations, there is no longer a trivial steady state, algebraic solution, and therefore the steady state and transient parameters are fit simultaneously to one set of steady state data, and six sets of steps up/down in shear rate data. (We note here that the values reported in Table VII, are analogous to those previously reported for the sake of comparison, with respect to order of magnitude, units, etc.). Fig. 6 shows the model predictions to the SAOS amplitude sweep. LAOS and UDLAOS predictions are shown below in the model comparison section. We note that t-ETV N1 predictions are shown in Appendix B, along with all contributions to total stress from plasma and RBCs and the buildup and breakdown of the rouleaux.

FIG. 5 t-ETV model fit for (a) steady state human blood data; (b) set of 3 step-up in shear rate from &of $0.1s^{-1}$ to 5, 10, and $20s^{-1}$; (c) corresponding structure parameter curves (colors of structure parameter curves match respective colors from stress evolution curves); (d) step-down in shear rate to &of $0.1s^{-1}$ from 5, 10, and $20s^{-1}$; and (e) corresponding structure parameter curves (Donor3) (dataset3) [55].

FIG. 6 Small amplitude oscillatory shear, amplitude sweep performed at $\omega = 12.6\,(\mathrm{rad/s})$, data discrete point, and predictions, dashed lines of t-ETV (Donor3) (dataset3) [55].

Table VII: Best fit parameter values of t-ETV model for Donors 1-5 [52-57] (F_{cost} steady state and step-up/downs dimensionless; $F_{cost,SAOS}$ has units of (Pa)).

t-ETV (Tensorial)								
	Par.	**Donor1**	**Donor2**	**Donor3**	**Donor4**	**Donor5**	**Ave.**	**Stdev**
SS	$\mu_{0,c}$ **(Pa s)**	0.0079	0.0079	0.0078	0.0074	0.0101	0.0082	0.00107
	$\mu_{\infty,c}$ **(Pa s)**	0.0032	0.0033	0.0033	0.0035	0.0037	0.0034	0.00021
	τ_C **(s)**	0.049	0.049	0.029	0.043	0.065	0.0474	0.01278
	τ_{break} **(s)**	0.859	0.871	1.147	1.086	0.966	0.9860	0.12808
	τ_{aggr} **(s)**	5.85E-04	6.49E-04	4.12E-02	1.60E-02	1.53E-05	1.17E-02	1.78E-02
	μ_R **(Pa s)**	0.038	0.033	0.032	0.047	0.045	0.0390	0.00703
	σ_{y0} **(Pa)**	0.0012	0.0023	0.0036	0.0022	0.0027	0.0024	0.00085
	$\gamma_{0,R}$ **(-)**	1	1	1	1	1	-	-
	d (-)	1/2	1/2	1/2	1/2	1/2	-	-
	m (-)	3/2	3/2	3/2	3/2	3/2	-	-
	F_{cost} **(SS)***	**0.0123**	**0.0115**	**0.0123**	**0.0078**	**0.0075**	**0.0103**	**0.00241**
trans, t-ETV	τ_λ **(s)**	1.3521	1.8571	1.7941	2.7851	2.1211	1.9819	0.5272
	G_R**(Pa)**	0.1599	0.1480	0.2117	0.1166	0.1397	0.1552	0.0354
	G_c **(Pa)**	0.4620	0.4058	0.8329	0.3801	0.6547	0.5471	0.1926
	F_{cost} **(trans)***	**0.0190**	**0.0197**	**0.0176**	**0.0173**	**0.0130**	**0.01732**	**0.0026**
	Fcost (SAOS)	**0.0023**	**0.0021**	**0.0023**	**0.0012**	**0.0018**	**0.00194**	**0.0005**

D. t-ESSTV

The t-ESSTV full tensor has the same number of parameters as the t-ETV, with a total of thirteen parameters fit simultaneously to steady state and six steps up/down in shear rate experiments. As before three of the thirteen parameters are fixed: $\gamma_{0,R}$ set to one, as in previous sections [7-9, 36, 37, 42, 43]; with the same values as previously mentioned for *d* and *m*. Fig. 7(a) shows the steady state fit, and Fig. 7(b) and (d) show the fit to the three step-down and three step-

ups in shear rate, respectively. Fig. 7(c) and (e) are showing the corresponding evolution of the structure parameter during the step down and step up in shear rate experiments. Table VIII shows the best fit model parameters from the steady state and transient data fit, and the value of $F_{cost,ss}$ for the steady state, step up/downs and dimensional F_{cost} of SAOS for Donor 3 (Donor 1-5 average F_{cost} values for SAOS, LAOS and UDLAOS predictions are shown in Table X). (We note here that the values reported in Table VIII, are analogous to those reported in the other tables for the sake of comparison). Fig. 8 shows the model predictions to the SAOS amplitude sweep. LAOS and UDLAOS predictions are shown below in the model comparison section. We note that t-ESSTV N1 predictions are shown in Appendix B, Fig. B1, along with all contributions to total stress from plasma and RBCs and the buildup and breakdown of the rouleaux in Fig. B2.

FIG. 7 t-ESSTV tensor model fit for (a) steady state human blood data; (b) set of 3 step up in shear rate from $\dot{\gamma}$ of $0.1s^{-1}$ to 5, 10, and $20s^{-1}$; (c) corresponding structure parameter curves (colors of structure parameter curves match respective colors from stress evolution curves); (d) step down in shear rate to $\dot{\gamma}$ of $0.1s^{-1}$ from 5, 10, and $20s^{-1}$; and (e) corresponding structure parameter curves (Donor3) (dataset3) [55].

FIG. 8 Small amplitude oscillatory shear, amplitude sweep performed at $\omega = 12.6(\mathrm{rad/s})$, data discrete point, and predictions, dashed lines of t-ESSTV (tensor) (Donor3) (dataset3) [55].

Table VIII: Best fit parameter values of t-ESSTV model for Donors 1-5 [52-57] (F_{cost} dimensionless).

t-ESSTV (Tensorial)								
	Par.	**Donor1**	**Donor2**	**Donor3**	**Donor4**	**Donor5**	**Ave.**	**Stdev**
SS	$\mu_{0,c}$ **(Pa s)**	0.0079	0.0067	0.0074	0.0076	0.0095	0.0078	0.00104
	$\mu_{\infty,c}$ **(Pa s)**	0.0033	0.0032	0.0034	0.0035	0.0038	0.0035	0.000216
	τ_C **(s)**	0.048	0.029	0.030	0.044	0.065	0.0431	0.01492
	τ_{break} **(s)**	0.869	1.143	1.157	1.084	0.970	1.0446	0.122671
	τ_{aggr} **(s)**	5.72E-04	4.29E-02	4.32E-02	1.64E-02	1.62E-03	2.09E-02	2.11E-02
	μ_R **(Pa s)**	0.035	0.036	0.033	0.045	0.044	0.0384	0.005393
	σ_{y0} **(Pa)**	0.002	0.003	0.004	0.002	0.003	0.0029	0.000794
	$\gamma_{0,R}$ **(-)**	1	1	1	1	1	-	-
	d (-)	1/2	1/2	1/2	1/2	1/2	-	-
	m (-)	3/2	3/2	3/2	3/2	3/2	-	-
	F_{cost} **(SS)***	**0.0074**	**0.0061**	**0.0103**	**0.0057**	**0.0059**	**0.0071**	**0.001944**
trans, t-ESSTV	τ_λ **(s)**	0.9966	1.1598	1.3052	1.3086	1.1766	1.1893	0.1283
	G_R**(Pa)**	0.0782	0.1056	0.1181	0.0985	0.1001	0.1001	0.0144
	G_c **(Pa)**	0.6437	0.5674	1.0052	0.5952	0.6888	0.7001	0.1768
	F_{cost} **(trans)***	**0.0150**	**0.0172**	**0.0143**	**0.0118**	**0.0120**	**0.01404**	**0.0022**
	Fcost (SAOS)	**0.0005**	**0.0014**	**0.0008**	**0.0010**	**0.0013**	**0.00100**	**0.0004**

Table IX: F_{cost} for fits, and predictions of all models for Donor3 [52-57] (F_{cost} for step up/down shown with dimensions of stress, as it is developed for stress predictions, and in a dimensionless scaled form (indicated by *) for comparison)

Donor3				
F_{cost} **(Pa)**	**ESSTV**	**t-ESSTV**	**ETV**	**t-ETV**
SS*	0.0135	0.0103	0.0102	0.0123
Step Up/Down*	0.0214	0.0143	0.0204	0.0176
Step Up/Down	0.000836	0.000580	0.000811	0.000677
SAOS	0.00183	0.00081	0.00341	0.00228
LAOS	0.00190	0.00189	0.00190	0.00156
UDLAOS	0.00132	0.00098	0.00132	0.00121
SUM	**0.00590**	**0.00426**	**0.00745**	**0.00572**

We note that according to the F_{cost} value comparison from Table V to Table VIII there is a modest improvement in predictive capability with respect to the step up/down in shear rate accuracy, for both the ETV and ESSTV, in applying the full tensor approach. While there is more significant accuracy improvement with the SAOS predictions, as shown in Table IX. With the

ability to fit steady state slightly worse with the respective tensorial versions of the ETV. The LAOS and UDLAOS predictions using the tensorial form of the respective models also shows improvement for Donor3. Similar trends are shown below with respect to the relative accuracy for the *average* SAOS, LAOS and UDLAOS predictions of Donors 1-5 shown in Table X. Table IX, and Table X demonstrate that by moving to the tensor form of the model we can increase predictive capability of the ETV and ESSTV rheological models. Without the addition of more parameters.

E. Comparison

Table VIII above offers a comparison of the cost functions of the steady state and transient fits for Donor3, while Table IX below shows a comparison for the SAOS, LAOS and UD-LAOS predictions for all models together, over all Donors. Fig. 9 shows the elastic and viscous projections for the LAOS and UDLAOS predictions with the non-tensorial versions of the models, while Fig. 10 shows the elastic and viscous projections for the LAOS and UDLAOS predictions with the tensorial versions. Table IX below has the $F_{cost,\,\mathrm{LAOS}}$ and $F_{cost,\,\mathrm{UDLAOS}}$ for each of the predictions for comparison between experiments, with average values for each shown at the bottom of Table IX. From Table IX two things are clear: 1. The ETV and ESSTV have similar accuracy demonstrated for each of the rheological experiments fit or predicted here; and 2. There is significant gains in accuracy shown by upgrading to the full tensor version for both models, with no additional cost in parameters.

With respect to I_3/I_1 data and model predictions shown in Figs. 2, 4, 6, and 8, due to the work of Horner et al. we believe we can rule out the skin effect from drying/clotting blood at the outer edge of the rheometer due to the extremely small ratio of surface area in contact with the surrounding air to surface area of the double wall Couette with the blood inside the cup and double

wall Couette geometry [40]. Furthermore, a cover is incorporated to minimize evaporation effects. We therefore support the hypothesis that it is the small values of elastic moduli relative to the values of the viscous moduli. We believe that due to the complicated nature of human blood physiology that the materials are intrinsically non-linear. Accordingly, the human blood has at least three different, yet overlapping time scales: 1. The viscoelastic time scale associated with the plasma and individual red blood cells; 2. The viscoelastic time scale associated with the contribution to total stress from rouleaux; and 3. The 'overall' timescale that governs rouleaux build-up and break-down. This last one can be further analyzed as resulting from the combination of three characteristic time scales, $\tau_\lambda, \tau_{break}$ and τ_{aggr}, the first one corresponding to the Brownian aggregation time scale and the last two used to define the dimensionless Weissenberg numbers that modify this time scale to define the shear-induced breakage and aggregation events. Yet to be considered is also the possibility that there is yet another independent time scale for the contribution to the total stress from the 'solid-like' stretching, elastic stress from the rouleaux before they undergo break-down. There are strong arguments in favor of the intrinsic non-linearity of human blood for these reasons [40].

With respect to the elastic and viscous projections all the models can capture qualitatively the LAOS and UDLAOS behavior. We note here that at the higher frequency and strain amplitudes for both LAOS and UDLAOS the human blood is almost entirely a viscous signature but does show signs of more elasticity present at the lower values of strain amplitude. In general, we also note that all four of the models shown here can quantitatively predict the stress signatures at the higher values of frequency and strain amplitude, in places where the blood is almost completely liquified, and the rouleaux are not able to form and stay together in large numbers, aka. the structure is almost completely broken down. According to Table IX we see that the ESSTV, and

t-ESSTV slightly outperform their counterparts ETV and t-ETV. This is seen quantitatively in the fits and predictions, as well as shown qualitatively in Figs. 9-10.

Lastly, it is useful to point out here that from a comparison of the τ_{break} and τ_{aggr} parameter values, shown in Tables V-VIII, one can see that for all donors the corresponding Wi_{break} is always 2- 4 orders of magnitude greater to Wi_{aggr}. This observation, in addition to the fact that the effect of the latter is further diminished having to take its square root in the kinetic equation for λ, Eq. (10), is consistent to the experimental observation that shear-induced aggregation is the lesser of the three effects modeled, giving further credibility to the models utilized in this work.

Fig. 9 (a-b) Elastic and viscous LAOS projections of ETV (blue lines); (c) elastic and viscous uni-directional LAOS ETV projections (blue lines); (e-f) elas viscous LAOS projections of ESSTV (maroon lines); (g) elastic and viscous uni-directior ESSTV projections (maroon lines

γ_0 (-)

Fig. 10 (a-b) Elastic and viscous LAOS projections of t-ETV(black lines); (c) elastic and viscous uni-directional LAOS t-ETV projections (black lines); (e-f) elastic and viscous LAOS projections of t-ESSTV(green lines); (g) elastic and viscous uni-directional LAOS tensorial t-ESSTV(green lines); Red points are data; x-axis is frequency (rad/s), y-axis is strain amplitude (-) (Donor 3) [55]. All solid lines are model predictions.

Table IX below shows significant improvements to LAOS and UDLAOS predictive capability with respect to both tensorial versions of the ETV and ESSTV models, respectively. This is shown for Donor 3 predictions in Figs. 9-10, and Table IX shows that this trend is maintained over Donors 1-5. Table IX shows the average of all categories of F_{cost} for each of the

five Donors, with an average sum of all the dimensional F_{cost} values accumulated and shown at the bottom of the table.

TABLE X. Comparison of average F_{cost}, for all models over fits (steady state and step up/down in shear rate) and predictions (SAOS, LAOS and UDLAOS) (average of ***five*** Donors). Note: the tensor model ΣF_{cost} were averaged and summed over 3 donors. (*The steady state F_{cost} values shown here are nondimensional, normalized by stress values at each respective shear rate of the flow curve).

Donors1-5 (Average)				
Fcost (Pa)	**ESSTV**	**t-ESSTV**	**ETV**	**t-ETV**
SS*	0.00839	0.00707	0.00883	0.01029
Step Up/Down*	0.01569	0.0145	0.02012	0.01732
Step Up/Down	0.00061	0.00054	0.00081	0.00064
SAOS	0.00157	0.00087	0.00231	0.00194
LAOS	0.00214	0.00193	0.00191	0.00212
UDLAOS	0.00252	0.00211	0.00238	0.00264
SUM	**0.00685**	**0.00545**	**0.00741**	**0.00734**

V. CONCLUSIONS

We have demonstrated a new paradigm for TEVP modeling using the original ethixo mHAWB as a starting point. We removed the plastic shear rate, $\dot{\gamma}_p$ from the constitutive equation for viscoelastic stress from rouleaux and replaced this with $\dot{\gamma}$ total shear rate. We then used for the elastoviscoplastic contribution to total stress from the rouleaux an equation inspired by recent work by Varchanis et al. [36], Wei et al. [37], and Armstrong et al. [43]. Both proposed tensorial frameworks allowed for a seamless transition to a full tensorial approach in modeling with the ETV and ESSTV, thus achieving improvements in the predictive capability for LAOS and

UDLAOS to that of the original ethixo mHAWB. The improvement in predictive capability by transitioning to the full tensorial version of both models was significant, and the key finding of this effort. It is noteworthy that the t-ETV construct lends itself to a full casting into a thermodynamically consistent model moving forward [26].

It is now clear that to effectively model the rheological flow of human blood, three components are required, each with a requisite number of parameters to capture the appropriate physics: 1. viscoelastic contribution to total stress from individual cell deformation within the plasma, here modeled with the White-Metzner utilizing the Cross model to describe the viscosity as a function of the shear rate (four fit parameters); 2. viscoelastic contribution to total stress from rouleaux modeled here in two distinct strategies using either the Saramito/Wei et al./ Varchanis et al. theory of plasticity inspired term or the Horner et al. framework (three fit parameters) [9, 10,]; and 3. the shear breakage, shear aggregation and Brownian aggregation of the rouleaux (three fit parameters) [31, 35, 36, 37].

With respect to recent advancements in thixo-elasto-visco-plastic modeling efforts we have demonstrated here a unique way to achieve gains in fitting and predictive capability without the addition of more, or new parameters [7-9, 41, 43]. This upgrade in accuracy was demonstrated for two modified versions of the contemporary mHAWB model by Horner et al. [8, 9]. There was a slight modification in the physics, etc. shown here, or parameters tied to physics, or fitting parameters. By upgrading to a full tensorial approach modeling blood rheology has evolved further with respect to accuracy without the addition of new parameters. Moving forward it will be highly desirable to use the TEVP models for more than a scalar representation of current levels of microstructure, and we aim to evolve the modeling shown here to a conformation tensor basis. In addition, more experimental results under conditions under which the thixotropic properties of

blood are most prevalent (like in stress relaxation) are highly desirable. The scalar structure parameter will still need to be incorporated in future models. Any parameters incorporated will have more value if they are directly tied to actual physics of microstructure evolution, and/or viscoelastic properties such as viscosity, elastic modulus, and yield stress.

APPENDIX A: TEVP MODEL ACRONYMS AND BRIEF DESCRIPTIONS

Acronym	Title	Brief Description
IH	isotropic hardening	internal dimensionless structure parameter [33]
KH	kinematic hardening	deformation dependent yield stress [34, 35]
HAWB	Horner Armstrong Wagner Beris	White-Metzner-Cross for plasma + contribution from yield stress and rouleaux
mHAWB	modified Horner Armstrong Wagner Beris	White-Metzner-Cross for plasma + contribution from yield stress + VE contribution from rouleaux
ethixo mHA	enhanced thixotropy term + mHAWB	(same has mHAWB) + thixotropic evolution with shear aggregation term
ETV	enhanced thixoviscoelastic	White-Metzner-Cross for plasma+e. thixotropy & removal of plastic shear rate from VE-rouleaux
ESSTV	enhanced structural stress thixoviscoelastic	White-Metzner-Cross for plasma+enhanced thixotropy & theories of plasticity
ML-IKH	Multimode-lambda + isotropic/ kinematic hardening	Multimode lambda evolution + theories of plasticity
SPTT-IKH	Saramito-Phan-Thien-Tanner + isotropic/ kinematic hardening	Saramito and Phan-Thien-Tanner description + theories of plasticity

APPENDIX B: STEADY STATE N1 PREDICTIONS OF t-ETV AND t-ESSTV

Fig. B1 shows the N1 prediction of the steady state data with the tensorial versions of the ESSTV and the ETV models. From this figure there is a considerable difference between the two models at low shear rates. We believe that this difference arises because of the viscoplastic

framework of the t-ESSTV model that incorporates $\left|\tilde{\sigma}-\left(\frac{\sigma_{y0}}{\gamma_{0,R}}\right)\|\gamma_e\|\right|$, a term involving the total (elastic plus viscoelastic) rouleaux stresses, in the numerator of the conditional for the stress. This contributes to the unique shape of the N1 prediction curve. The t-ETV has a different formulation for the viscoelastic rouleaux contribution, which does not involve the elastic contribution to the total stress, as shown in Tables I and II. .

FIG. B1 N1 predictions for steady state of t-ESSTV and t-ETV for Donor3 (dataset3) [55].

Fig. B2 Below shows the individual contributions to total stress using t-ETV and t-ESSTV models respectively from a step-up ($\dot{\gamma}_i=0.1s^{-1} \rightarrow \dot{\gamma}_f=20s^{-1}$) , and a step-down ($\dot{\gamma}_i=20s^{-1} \rightarrow \dot{\gamma}_f=0.1s^{-1}$) in shear rate test. Fig. B2a,b shows the data, total stress, and the viscoelastic contribution to total stress from the plasma and individual RBCs, the rouleaux and the elastic contributions to total stress from rouleaux of the t-ETV model. Fig. B2c,d show the data, total stress, and the viscoelastic contribution to total stress from the plasma and individual RBCs, and the rouleaux of the t-ESSTV model. Note that the t-ESSTV lacks a prediction for the elastic contribution from the rouleaux. For reference the N1 predictions are shown for both models.

FIG. B2 (a,b) Contribution to total stress from plasma and RBCs (green dash-dot line), contribution to total stress from rouleaux (red solid line), contribution to total stress from elastic stress of rouleaux (blue solid line), total stress (wine dash line) and N1 predictions (black solid line) of t-ETV; and (c,d) Contribution to total stress from plasma and RBCs (red dash-dot line), contribution to total stress from rouleaux (green dash-dot line), total stress (aqua line) and N1 predictions of t-ESSTV. (a,c) step up in shear rate from $0.1s^{-1}$ to $20s^{-1}$; (b,d) step down in shear rate from $20s^{-1}$ to $0.1s^{-1}$. (Data is maroon squares.) Donor3 (dataset3) [55]

APPENDIX C: Hysteresis Loops of Donor 3

Fig. B3a shows a hysteresis loop of Donor 3 for a combination of α and t_{max}, where in Eqn. 35 below, t is time, t_{max} is maximum time of experiment, and α is the non-dimensional acceleration constant. The triangle ramp, or hysteresis experiment, started at time t=0 (s) from rest, continuously increases in shear rate until a maximum is reached at $t=\frac{t_{max}}{2}$, followed by a decreasing shear rate back to 0 s^{-1}. Whereby the thixotropic timescale of rouleaux breakdown, is demonstrated to be different than the characteristic timescale of rouleaux buildup

$$\dot{\gamma}(t)=\begin{cases}\alpha t & t\le\frac{t_{max}}{2}\\ \alpha\left(t_{max}-t\right) & t>\frac{t_{max}}{2}\end{cases}. \tag{35}$$

Fig. C1a,b shows the characteristic hysteresis loop, and compares the ETV, ESSTV and a viscoelastic model that does not have a thixotropic term, Stickel et al. elasto-visco-plastic model highlighted here [47, 58]. The Stickel et al. EVP model consists of 4 model parameters, and the following two equations

$$\sigma=\sigma_{y0}+k\dot{\gamma}^{n}, \tag{36}$$

and

$$\frac{1}{G}\dot{\sigma}+\max\left(0,\frac{|\sigma|-\sigma_{y0}}{k|\sigma|^{n}}\right)^{1/n}\sigma=\dot{\gamma}. \tag{37}$$

Where k is the consistency parameter, n is the power law, and σ_{y0} is the yield stress. We again fit the parameters in Eqn. (36) to steady state data, and G, the elastic modulus from Eqn. (37) is fit to six sets of step-up/down in shear rate data for a fair comparison. The results of the

parameter fitting are shown in Fig. C2. The comparison in Fig. C1 is shown with the non-tensorial versions ETV, and ESSTV for a fair comparison to the Stickel et al. EVP model [47, 58]. Fig. C1a, and C2 both show significant loss in predictive capabilities without thixotropy term. Clearly if we try to use a viscoelastic only model, like that of Stickel et al. [58], the time constants resulting from best fit of the steady state and step-up/down in shear rate (transient data) are too small to predict hysteresis as seen in Fig. C1. On the other hand, if you only have thixotropy (like the Apostolidis et al. [39]) we cannot do a good job predicting the nonlinear LAOS, and UDLAOS data. The only way to capture both the hysteresis and the nonlinear features of LAOS is to have both thixotropy and viscoelasticity in the model, both important for blood, as we shown with the ETV, ESSTV and their tensorial counterparts.

FIG. C1 Hysteresis loop for Donor 3 α=0.0357, t_{max}=35(s); data points as follows: $t<t_{max}/2$ maroon triangles, $t \geq t_{max}/2$ red circles; (a) Green line Stickel et al. [58] EVP model; and (b) Blue line ESSTV model; and black line ETV model. (Dashed lines represent $t < t_{max}/2$; solid lines represent $t \geq t_{max}/2$) (Numerals 1 – 4 are the stages of evolution of the hysteresis loop) (dataset3) [55], (Best fit parameter values: σ_{y0}=0.0058 (Pa); k=0.013; n=0.77; and G=1.64 (Pa)).

FIG. C2 Stickel et al. [58] EVP model fit (lines) for (a) steady state human blood data; (b) set of 3 step-up in shear rate from $\dot{\gamma}$ of $0.1s^{-1}$ to 5, 10, and $20s^{-1}$; and (c) step-down in shear rate to $\dot{\gamma}$ of $0.1s^{-1}$ from 5, 10, and $20s^{-1}$ for Donor 3, (dataset3) experimental data [55], (Best fit parameter values: σ_{y0}=0.0058 (Pa); k=0.013; n=0.77; and G=1.64 (Pa)).

NOMENCLATURE

Nomenclature	
ω	frequency of oscillation
γ_0	strain amplitude
t	time
λ	structure parameter
μ_{st}	rouleaux contribution to viscosity
μ_0	zero shear viscosity of plasma and RBC
μ_∞	infinite shear viscosity
G'	storage modulus
G"	loss modulus
G_R	elastic modulus of rouleaux
G_C	elastic modulus of plasma and RBC
σ_{y0}	yield stress
τ_{break}	material constant for stress-induced breakage
τ_{aggr}	material constant for stress-induced aggregation
τ_λ	thixotropic time constant of evolution
τ_C	Cross constant
σ	stress
$\dot{\gamma}$	shear rate (subscript p is plastic shear rate)
d	power law of shear aggregation
y_i	data value
f_i	model value
F_{cost}	cost function
$\boldsymbol{\gamma}_{(1)}$	rate of strain tensor
m	power law of rouleaux viscosity

Supplementary Material

ETV and ESSTV model fits of steady state and six step up/down in shear rate tests, with SAOS predictions of Donor1. Additional ETV LAOS and UDLAOS predictions with Donor1.

AUTHORS CONTRIBUTIONS

All authors contributed to this work.

ACKNOWLEDGEMENTS

The authors acknowledge the support and funding assistance from the U.S. Army, and the Department of Chemistry and Life Science, United States Military Academy. Dr. Jeff Horner facilitated the collection of the blood rheological data. Dr. Kevin O'Donovan provided significant insight into the physics of human blood flows, etc. Dr. Varchanis facilitated our exploration of models by providing mfiles to solve his SPTT-IKH model. The authors acknowledge the very insightful recommendations of the reviewers and editors of JOR. The views expressed herein are those of the authors and do not reflect the position of the United States Military Academy, the Department of the Army, or the Department of Defense. The authors acknowledge funding assistance from NSF CBET 1510837 which the blood was collected through. Norman Wagner, Antony Beris, Soham Jariwala acknowledge funding through NSF CBET 1804911.

DATA AVAILABILITY

The data that support the findings of this study are openly available in Mendeley at Mendeley.com at:

https://data.mendeley.com/datasets/ AUG18
https://data.mendeley.com/datasets/ jdzpx6hy6r/1, FEB19
https://data.mendeley.com/datasets/ , FEB20
https://data.mendeley.com/datasets/ s8w6s6f68b/1, NOV18
https://data/mendeley.com/datasets/ DEC18

REFERENCES

[1] Fahraeus, R., "The suspension stability of the blood," Physiol. Rev. **9**, 241–274 (1929).
[2] O. Baskurt, B. Neu, H. J. Meiselman, *Red Blood Cell Aggregation*. United States. CRC Press (2011).
[3] Schmid-Schonbein, H., P. Gaehtgens, and H. Hirsch, "On the shear rate dependence of red cell aggregation in vitro," J. Clin. Invest. **47**, 1447–1454 (1968).

[4] Merrill, E. W., E. R. Gilliland, G. Cokelet, H. Shin, A. Britten, and R. E. Wells, "Rheology of human blood, near and at zero flow," Biophys. J. **3**, 199–213 (1963).
[5] Thurston, G. B., "Viscoelasticity of human blood," Biophys. J.**12**, 1205–1217 (1972).
[6] Dintenfass, L., "Thixotropy of blood and proneness to thrombus formation," Circ. Res. **11**, 233–239 (1962).
[7] A. N. Beris, Chapter 8, Hemorheology, in: Theory and Applications of Colloidal Suspension Rheology, N.J. Wagner and J. Mewis (eds)., Cambridge U. Press, Cambridge, 2021, p.316-351.
[8] J. S. Horner, M. J. Armstrong, N. J. Wagner, A. N. Beris, "Investigation of blood rheology under steady and unidirectional large amplitude oscillatory shear," Journal of Rheology, **62(2)**, 577-591 (2018).
[9] J. S. Horner, M. J. Armstrong, N. J. Wagner, A. N. Beris, "Measurements of human blood viscoelasticity and thixotropy under steady and transient shear and constitutive modeling thereof," J. of Rheol. **63(5)**, 799-813 (2019).
[10] M. J. Armstrong and J. Tussing, "A methodology for adding thixotropy to Oldroyd-8 family of viscoelastic models for characterization of human blood," Physics of Fluids, **32**, 094111 (2020).
[11] Mauer, J., S. Mendez, L. Lanotte, F. Nicoud, M. Abkarian, G. Gompper, and D. A. Fedosov, "Flow-induced transitions of red blood cell shapes under shear," Phys. Rev. Lett. **121**, 118103 (2018).
[12] Schmid-Schonbein, H., and R. Wells, "Fluid drop-like transition of erythrocytes under shear," Science **165**, 288–291 (1969).
[13] Schmid-Schonbein, H., R. Wells, and J. Goldstone, "Influence of deformability of human red cells upon blood viscosity," Circ. Res.**15**, 131–143 (1969).
[14] Chien, S., "Biophysical behavior of red cells in suspensions," in The Red Blood Cell, edited by Douglas MacN. Surgenor, (Academic, New York, 1975), Vol. 2, Chap. 26, pp. 1032–1133.
[15] Lanotte, L., J. Mauer, S. Mendez, D. A. Fedosov, J. Fromental, V. Claveria, F. Nicoud, G. Gompper, and M. Abkarian, "Red cells' dynamic morphologies govern blood shear thinning under microcirculatory flow conditions," Proc. Natl. Acad. Sci. U.S.A. **113**, 13289–13294 (2016).
[16] Minetti, C., V. Audemar, T. Podgorski, and G. Coupier, "Dynamics of a large population of red blood cells under shear flow," J. Fluid Mech. **864**, 408–448 (2019).
[17] Chien, S., S. Usami, and J. F. Bertles, "Abnormal rheology of oxygenated blood in sickle cell anemia," J. Clin. Invest. **49**, 623–634 (1970).
[18] Letcher, R. L., S. Chien, T. G. Pickering, J. E. Sealey, and J. H. Laragh, "Direct relationship between blood pressure and blood viscosity in normal and hypertensive subjects: Role of fibrinogen and concentration," Am. J. Med. **70**, 1195–1202 (1981).
[19] Yarnell, J. W. G., I. A. Baker, P. M. Sweetnam, D. Bainton, J. R. O'Brien, P. J. Whitehead, and P. C. Elwood, "Fibrinogen, viscosity, and white blood cell count are major risk factors for ischemic heart disease: The Caerphilly and Speedwell collaborative heart disease studies," Circulation **83**, 836–844 (1991).
[20] Le Devehat, C., M. Vimeux, and T. Khodabandehlou, "Blood rheology in patients with diabetes mellitus," Clin. Hemorheol. Microcirc. **30**, 297–300 (2004).
[21] Lee, B., "Computational fluid dynamics in cardiovascular disease," Korean Circ. J. **41**, 423–430 (2011).
[22] Yilmaz, F., and M. Y. Gundogdu, "A critical review on blood flow in large arteries; relevance to blood rheology, viscosity models, and physiologic conditions," Korea-Aust. Rheol. J. 20, 197-211 (2008).

[23] Sequeira, A., and J. Janela, An overview of some mathematical models of blood rheology, in A Portrait of State-of-the-Art Research at the Technical University of Lisbon, edited by M. S. Pereira (Springer, Dordrecht, 2007).
[24] J. G. Oldroyd, "On the formulation of rheological equations of state," Royal Society of London 200(1063), 523-541 (1950).
[25] R. B. Bird, R. C. Armstrong, O. Hassager, Dynamics of polymeric liquids: Fluid mechanics, Vol. 1, 2nd Ed., United States. John Wiley and Sons Inc. (1987).
[26] A.N. Beris and B.J. Edwards (1994). Thermodynamics of Flowing Systems with Internal Microstructure, Oxford Univ. Press: New York.
[27] Barnes, A. H., "Thixotropy—A review," J. Non-Newtonian Fluid Mech. **70**, 1–33 (1997).
[28] Mujumdar, A., A. N. Beris, and A. B. Metzner, "Transient phenomena in thixotropic systems," J. Nonnewton. Fluid Mech. **102**, 157–158 (2002).
[29] Dullaert, K., and J. Mewis, "A structural kinetics model for thixotropy," J. Nonnewton. Fluid Mech. **139**, 21–30 (2006).
[30] Mewis, J., and N. J. Wagner, "Thixotropy," Adv. Colloid Interface Sci. **147–148**, 214–227 (2009).
[31] P. Saramito, "A new elastoviscoplastic model based on the Herschel-Bulkley viscoplastic model," J. Non-Newtonian Fluid Mech. **158**, 154-161 (2009).
[32] P. R de Souza Mendes, "Modeling the thixotropic behavior of structured fluids," J. Non-Newtonian Fluid Mech. **164**, 66–75 (2009).
[33] C. J. Dimitriou, R. H. Ewoldt, G. H. McKinley, "Describing and prescribing the constitutive response of yield stress fluids using large amplitude oscillatory shear stress (LAOStress)," J. Rheol. **57(1)**, 27-70 (2013).
[34] C. J. Dimitriou and G. H. McKinley, A comprehensive constitutive law for waxy crude oil: a thixotropic yield stress fluid, Soft Matter **10**, 6619–6644 (2014).
[35] C. J. Dimitriou and G. H. McKinley, A canonical framework for modeling elasto-viscoplasticity in complex fluids, J. Non-Newtonian Fluid Mech. **265**, 116-132 (2019).
[36] Y. Wei, M.J. Solomon, R.G. Larson, "A multimode structural kinetics constitutive equation for the transient rheology of thixotropic elasto-viscoplastic fluids," Journal of Rheology 62, 321 - 342 (2018).
[37] S. Varchanis, G. Makrigiorgos, P. Moschopoulos, Y. Dimakopoulos, J. Tsamopoulos, "Modeling the rheology of thixotropic elasto-visco-plastic materials," J. Rheol. **63**, 609-639 (2019).
[38] Phan-Thien N., and R. I. Tanner, "A new constitutive equation derived from network theory," J. Nonnewton. Fluid Mech. 2(4), 353–365 (1977).
[39] A. J. Apostolidis, M. J. Armstrong, A. N. Beris, "Modeling of human blood rheology in transient shear flows," J. Rheol. 59(1), 275-298 (2015).
[40] J. S. Horner, A. N. Beris, D. S. Woulfe, N. J. Wagner, "Effects of Ex Vivo Aging and Storage Temperature on Blood Viscosity," Clinical Rheology and Microcirculation, 70(2), 155-172 (2018).
[41] M. J. Armstrong, A. N. Beris, N. J. Wagner, "An Adaptive Parallel Tempering Method for the Dynamic Data-Driven Parameter Estimation of Nonlinear Models," AIChE Journal, Vol. 63, 1937-1958 (2016).
[42] M. Clarion, M. Deegan, T. Helton, J. Hudgins, N. Monteferrante, E. Ousley, and M. Armstrong, "Contemporary modeling and analysis of steady state and transient human blood rheology," Rheo. Acta **57(2)**, 141-168 (2018).

[43] M. Armstrong and A. Pincot, "Integration of thixotropy into Giesekus model for characterization of human blood", AIP Advances 11, 035029 (2021).
[44] H. Giesekus, "A simple constitutive equation for polymer fluids based on the concept of deformation-dependent tensorial mobility," J. of Non-Newtonian Fluid Mechanics 11(1-2), 69-109 (1982).
[45] M. J. Armstrong, A. N. Beris, S. Rogers, N. J. Wagner, "Dynamic shear rheology of a thixotropic suspension: Comparison of an improved structure-based model with large amplitude oscillatory shear experiments," J. of Rheol. 60(3), 433-450 (2016).
[46] M. Armstrong, J. Horner, M. Clark, M. Deegan, T. Hill, C. Keith, and Lynne Mooradian, "Evaluating rheological models for human blood using steady state, transient, and oscillatory shear predictions," Rheo. Acta 57(11), 705-728 (2018).
[47] M. Armstrong, M. Scully, M. Clark, T. Corrigan, C. James, "A simple approach for adding thixotropy to an elasto-visco-plastic rheological model to facilitate structural interrogation of human blood," Journal of Non-Newtonian Fluid Mech. 290, 104503 (2021).
[48] K. Giannokostas, P. Moschopoulos, S. Varchanis, Y. Dimakopoulos, J. Tsamopoulos, "Advanced constitutive modeling of the thixotropic elasto-visco-plastic behavior of blood: Description of the model and rheological predictions," Materials 13, 4184 (2020).
[49] M.Armstrong, K. Rook, W. Pulles, M. Deegan, and T. Corrigan, "Importance of viscoelasticity in the thixotropic behavior of human blood." Rheologica Acta, 60, 119-140 (2021).
[50] J. L. White and A. B. Metzner, "Development of constitutive equations for polymeric melts and solutions," J. Appl. Polym. Sci., 7, 1867–1889 (1963).
[51] Cross, M. M., "Rheology of non-Newtonian fluids: A new flow equation for pseudoplastic systems," J. Colloid Sci. 20, 417–437 (1965).
[52] A. Souvaliotis, and A.N. Beris, "An extended White-Metzner viscoelastic fluid model based on an internal structure parameter," J. Rheol. 36, 241–271 (1992).
[52] N.J. Wagner, J. Mewis, Theory and Applications of Colloidal Suspension Rheology, Cambridge University Press (2021).
[53] Dataset1 Matthew J. Armstrong, and Jeff S. Horner, AUG18 human blood rheology, (2021) DOI: 0.17632/sj6szsznr6.1.
[54] Dataset2 Matthew J. Armstrong, "FEB19 Blood Rheology ARESG2 SS, SAOS, LAOS, TRIANGLE RAMP, UDLAOS", Mendeley Data Sets 2020, DOI: 10.17632/8pbktvbx2z.1.
[55] Dataset3 Matthew J. Armstrong, and Jeff S. Horner, FEB20 human blood rheology, (2021) 10.17632/s672yykhf2.1
[56] Dataset4 Matthew J. Armstrong, and Jeff S. Horner, NOV18 human blood rheology, (2020) DOI: 10.17632/d9c6vk988t.1.
[57] Dataset5 Matthew J. Armstrong, and Jeff S. Horner, DEC18 human blood rheology, (2020) DOI: 10.17632/294cjj2hhj.1.
[58] J.J. Stickel, J. S. Knutsen, and M. W. Liberatore, "Response of elastoviscoplastic materials to large amplitude oscillatory shear flow in the parallel-plate and cylindrical Couette geometries," Journal of Rheology 57(6) , 1569-1596 (2013).

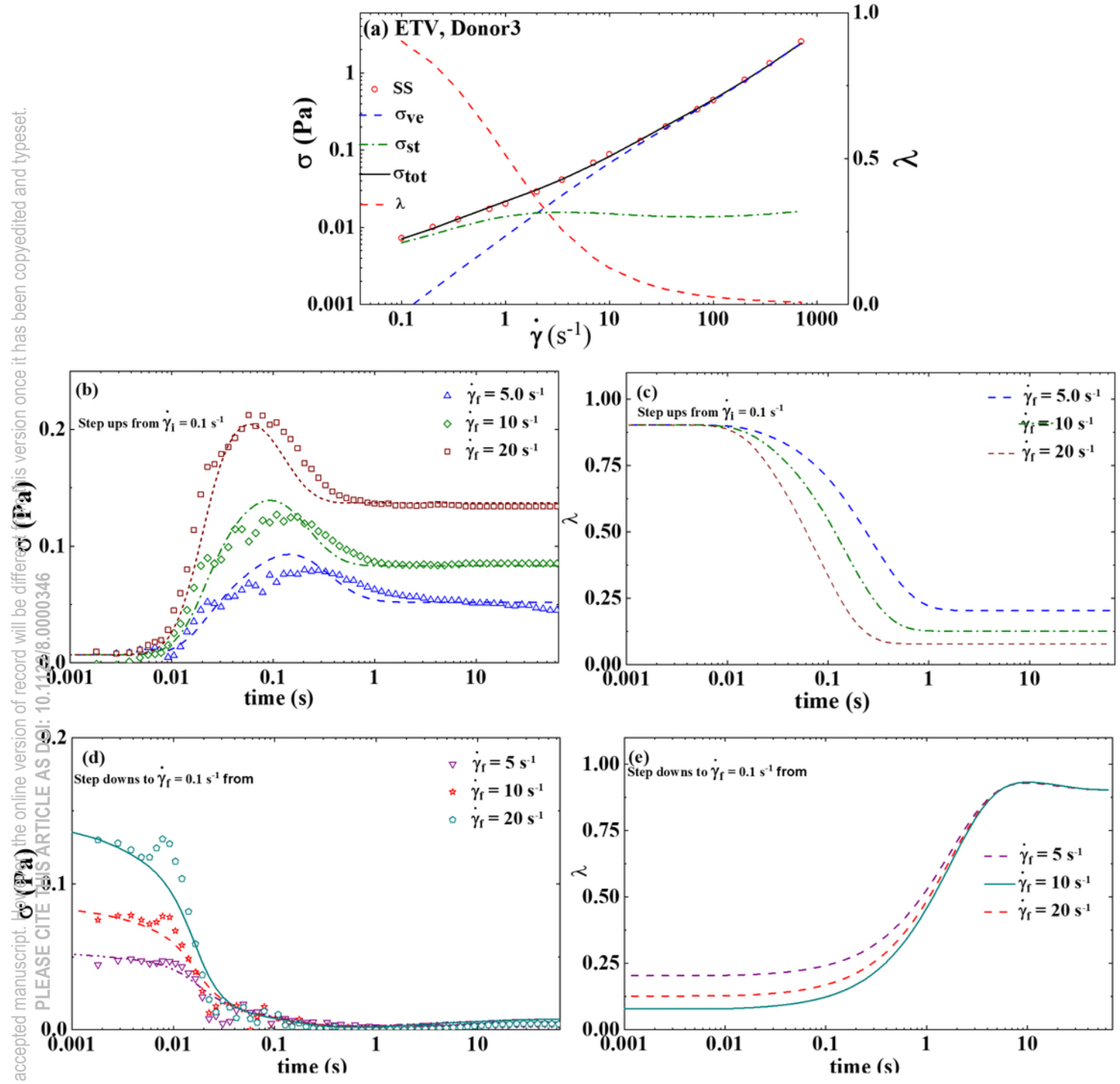

FIG. 1 ETV model fit for (a) steady state human blood data; (b) set of 3 step-up in shear rate from = 0.1s-1 to 5, 10, and 20s-1; (c) corresponding structure parameter curves (colors of structure parameter curves match respective colors from stress evolution curves); (d) step-down in shear rate to =0.1s-1 from 5, 10, and 20s-1 ; and (e) corresponding structure parameter curves (Donor3) (dataset3) [55].

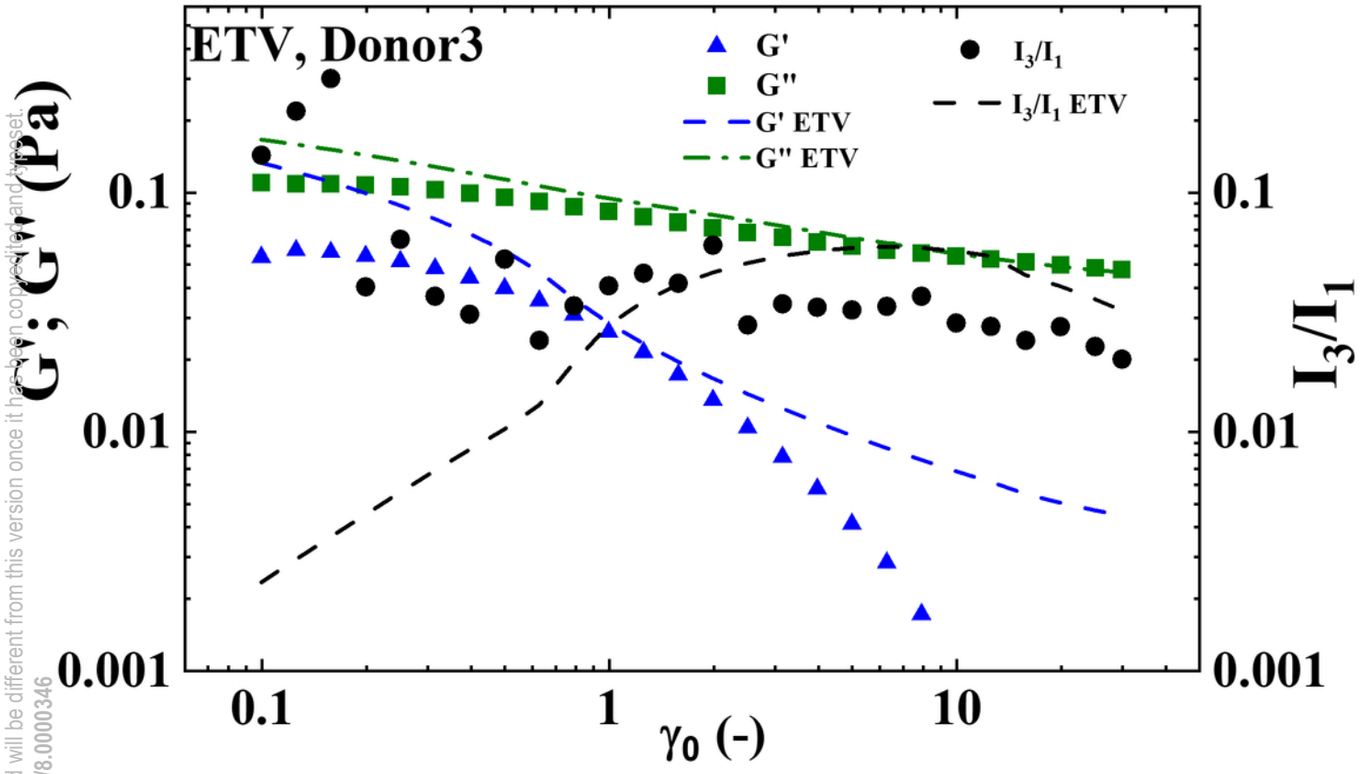

FIG. 2 Small amplitude oscillatory shear, amplitude sweep performed at, data discreet point, and predictions, dashed lines of ETV(Donor3) (dataset3) [55].

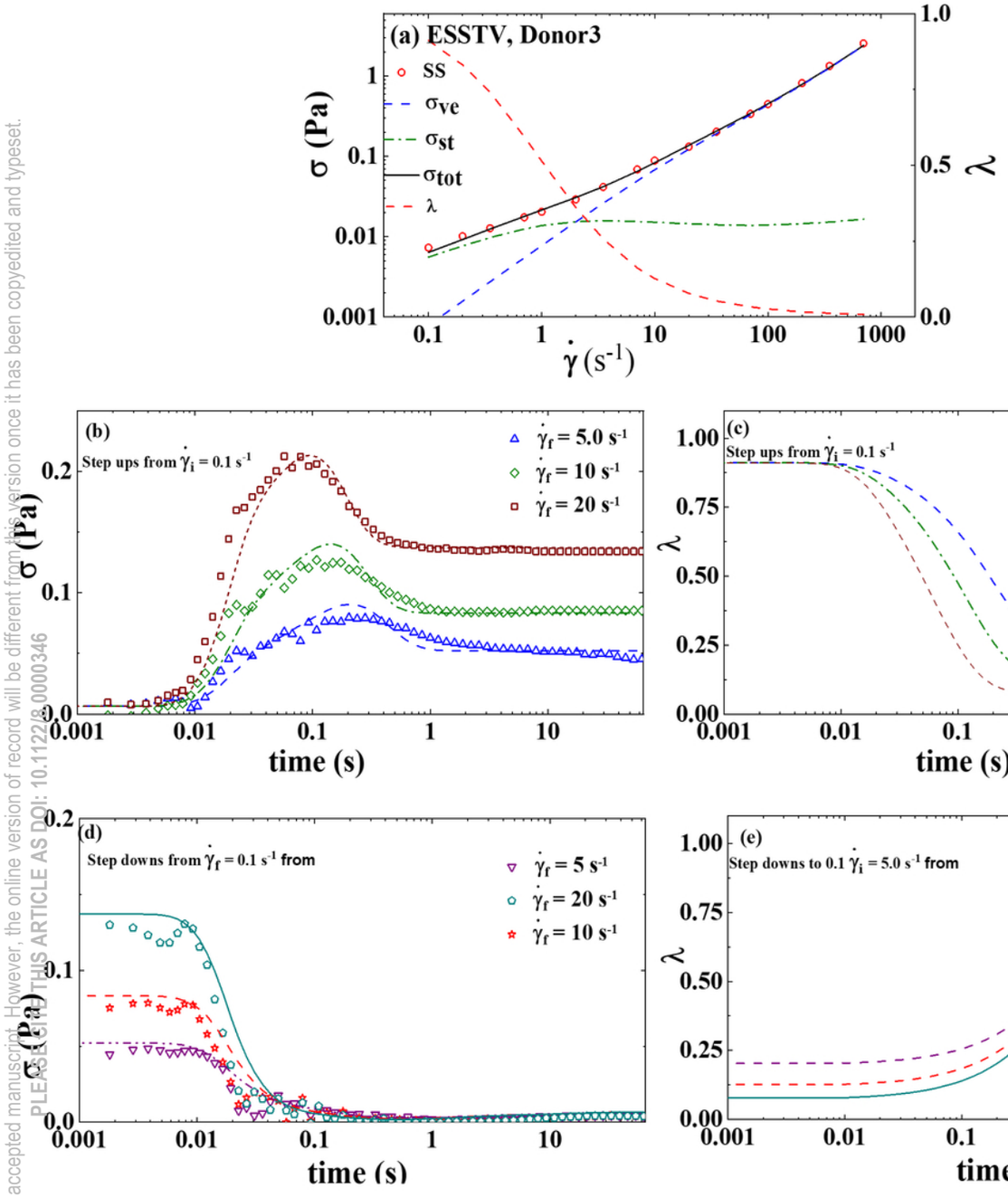

FIG. 3 ESSTV model fit for (a) steady state human blood data; (b) set of 3 step-up in shear rate from = 0.1s-1 to 5, 10, and 20s-1; (c) corresponding structure parameter curves (colors of structure parameter curves match respective colors from stress evolution curves); (d) step-down in shear rate to =0.1s-1 from 5, 10, and 20s-1 ; and (e) corresponding structure parameter curves (Donor3) (dataset3) [55].

Journal of Rheology

Journal of Rheology

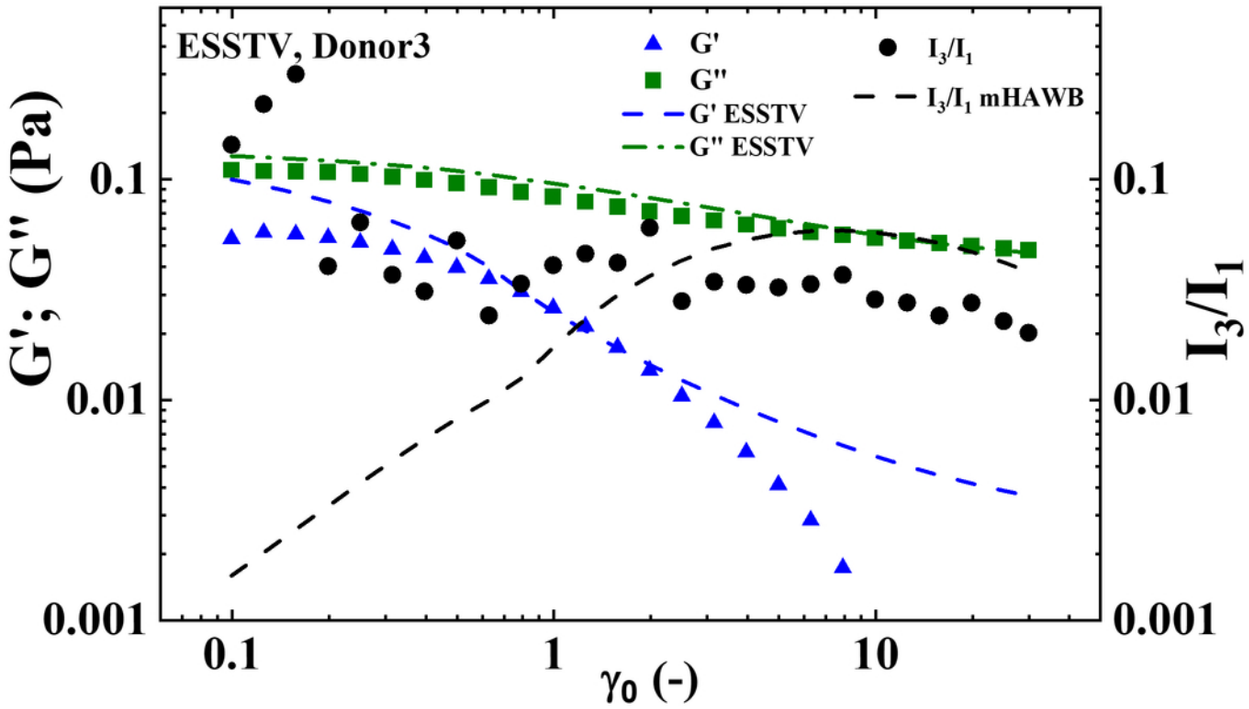

FIG. 4 Small amplitude oscillatory shear, amplitude sweep performed at , data discreet point, and predictions, dashed lines of ESSTV (Donor3) (dataset3) [55].

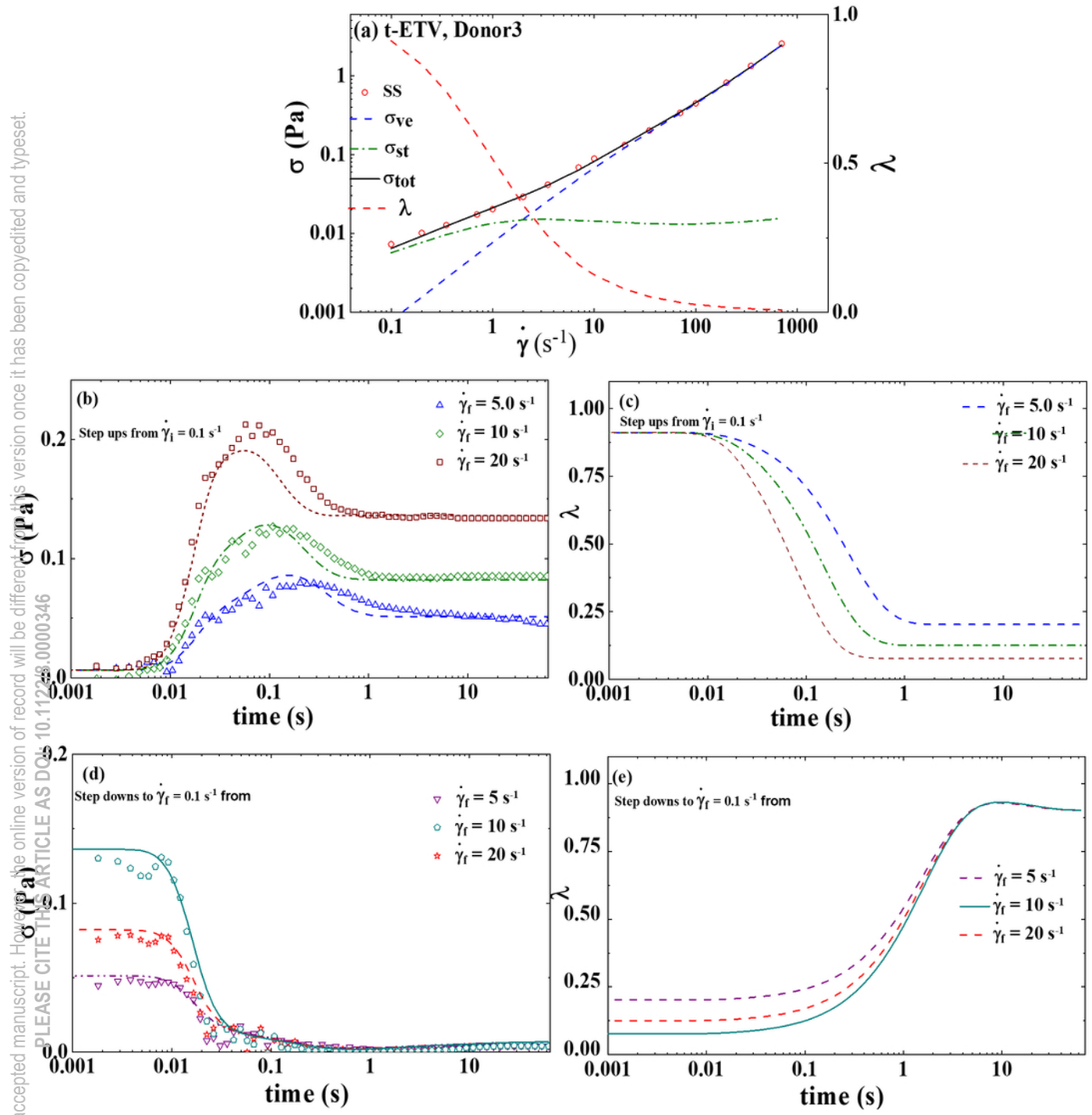

FIG. 5 t-ETV model fit for (a) steady state human blood data; (b) set of 3 step-up in shear rate from = 0.1s-1 to 5, 10, and 20s-1; (c) corresponding structure parameter curves (colors of structure parameter curves match respective colors from stress evolution curves); (d) step-down in shear rate to =0.1s-1 from 5, 10, and 20s-1 ; and (e) corresponding structure parameter curves (Donor3) (dataset3) [55].

Journal of Rheology

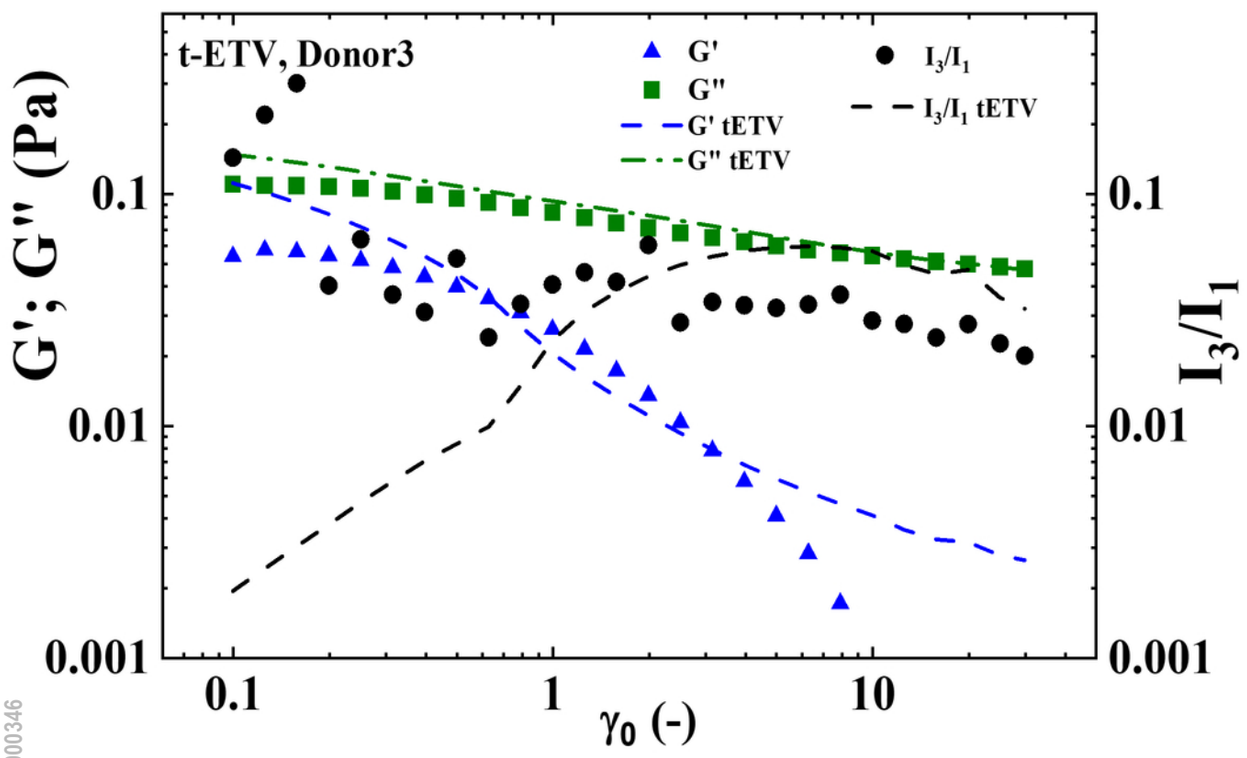

FIG. 6 Small amplitude oscillatory shear, amplitude sweep performed at , data discreet point, and predictions, dashed lines of t-ETV (Donor3) (dataset3) [55].

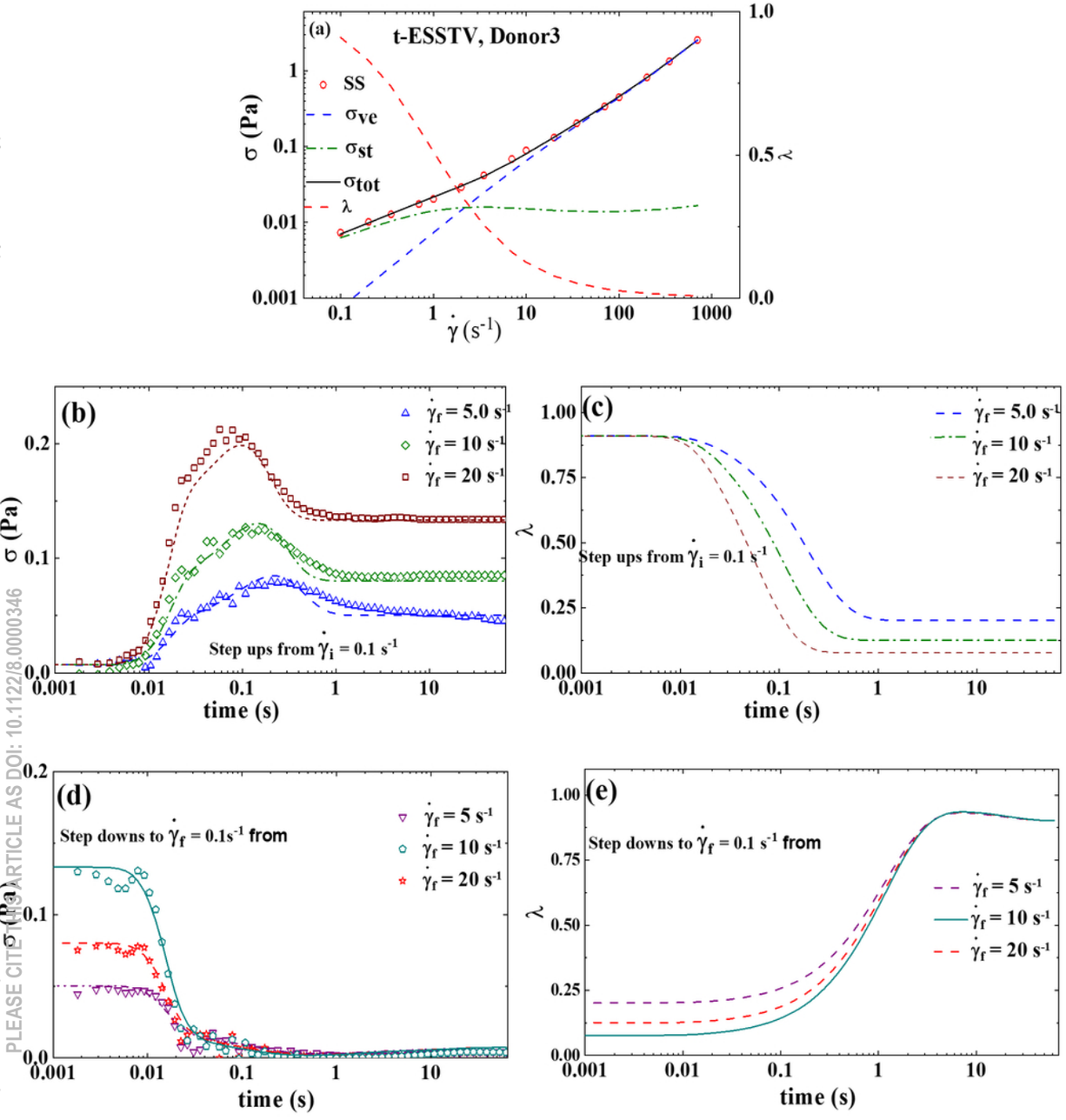

FIG. 7 t-ESSTV tensor model fit for (a) steady state human blood data; (b) set of 3 step up in shear rate from = 0.1s-1 to 5, 10, and 20s-1; (c) corresponding structure parameter curves (colors of structure parameter curves match respective colors from stress evolution curves); (d) step down in shear rate to =0.1s-1 from 5, 10, and 20s-1 ; and (e) corresponding structure parameter curves (Donor3) (dataset3) [55].

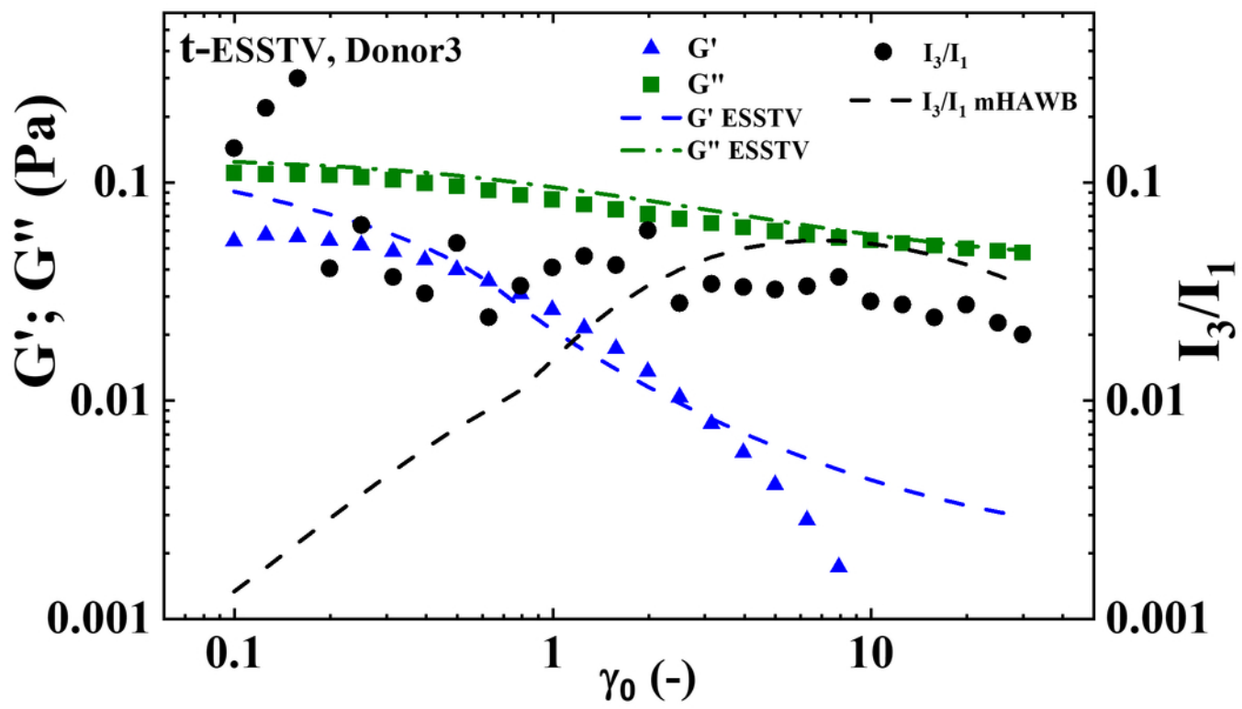

FIG. 8 Small amplitude oscillatory shear, amplitude sweep performed at , data discreet point, and predictions, dashed lines of t-ESSTV (tensor) (Donor3) (dataset3) [55].

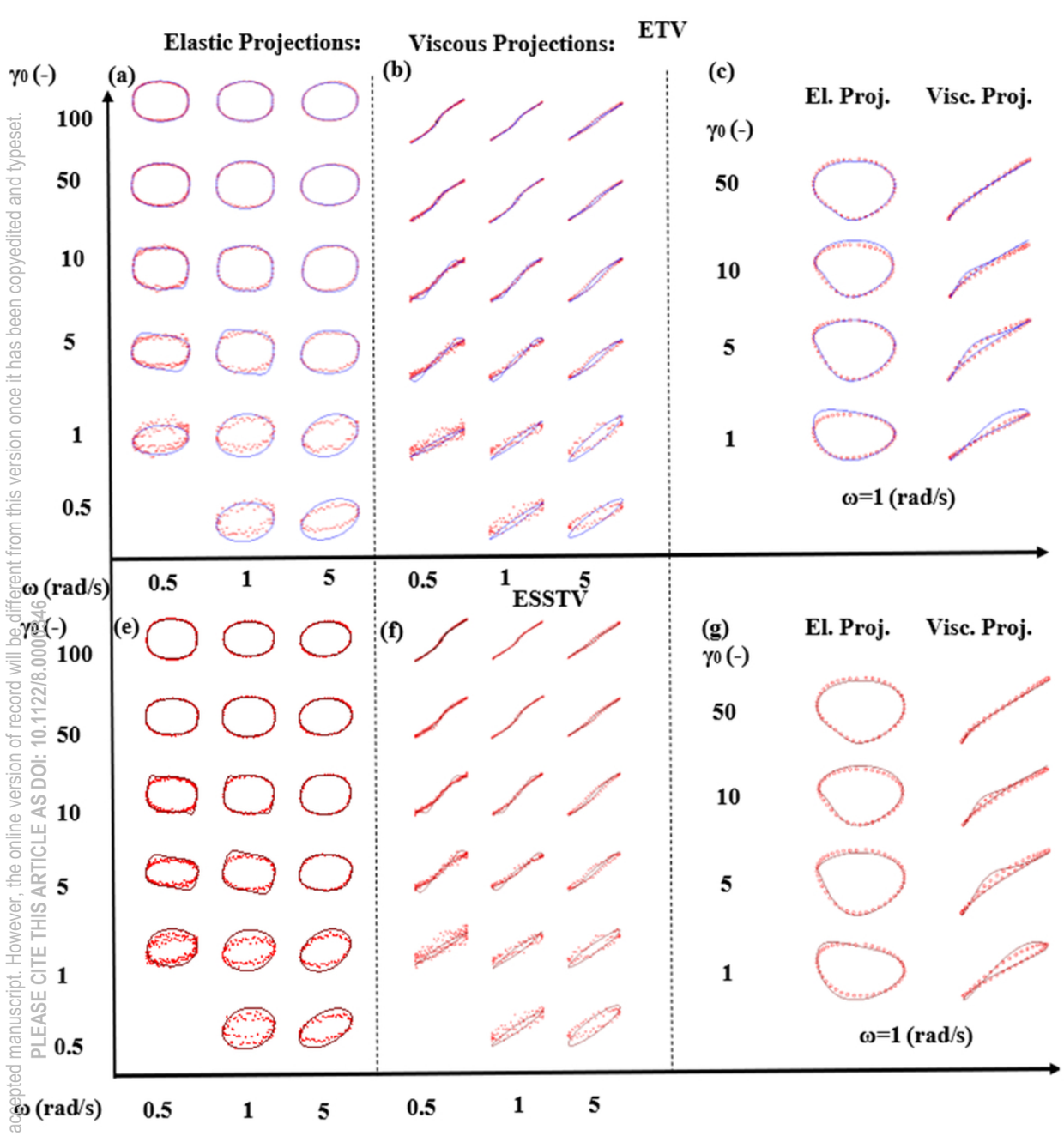

Fig. 9 (a-b) Elastic and viscous LAOS projections of ETV (blue lines); (c) elastic and viscous uni-directional LAOS ETV projections (blue lines); (e-f) elastic and viscous LAOS projections of ESSTV (maroon lines); (g) elastic and viscous uni-directional LAOS ESSTV projections (maroon lines); Red points are data; x-axis, frequency (rad/s), y-axis, strain amplitude (-) (Donor 3) [55].

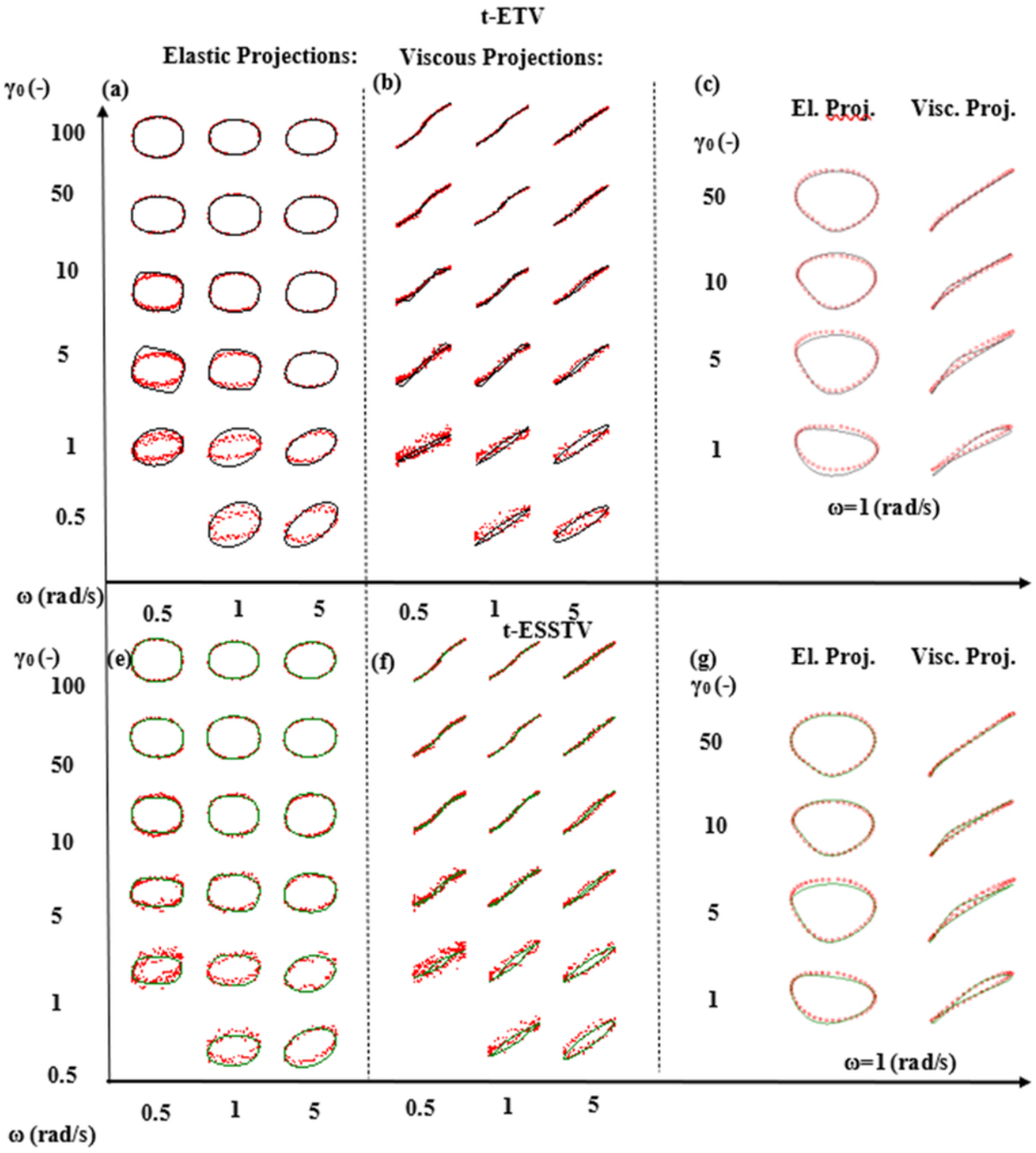

Fig. 10 (a-b) Elastic and viscous LAOS projections of t-ETV(black lines); (c) elastic and viscous uni-directional LAOS t-ETV projections (black lines); (e-f) elastic and viscous LAOS projections of t-ESSTV(green lines); (g) elastic and viscous uni-directional LAOS tensorial t-ESSTV(green lines); Red points are data; x-axis is frequency (rad/s), y-axis is strain amplitude (-) (Donor 3) [55]. All solid lines are model predictions.

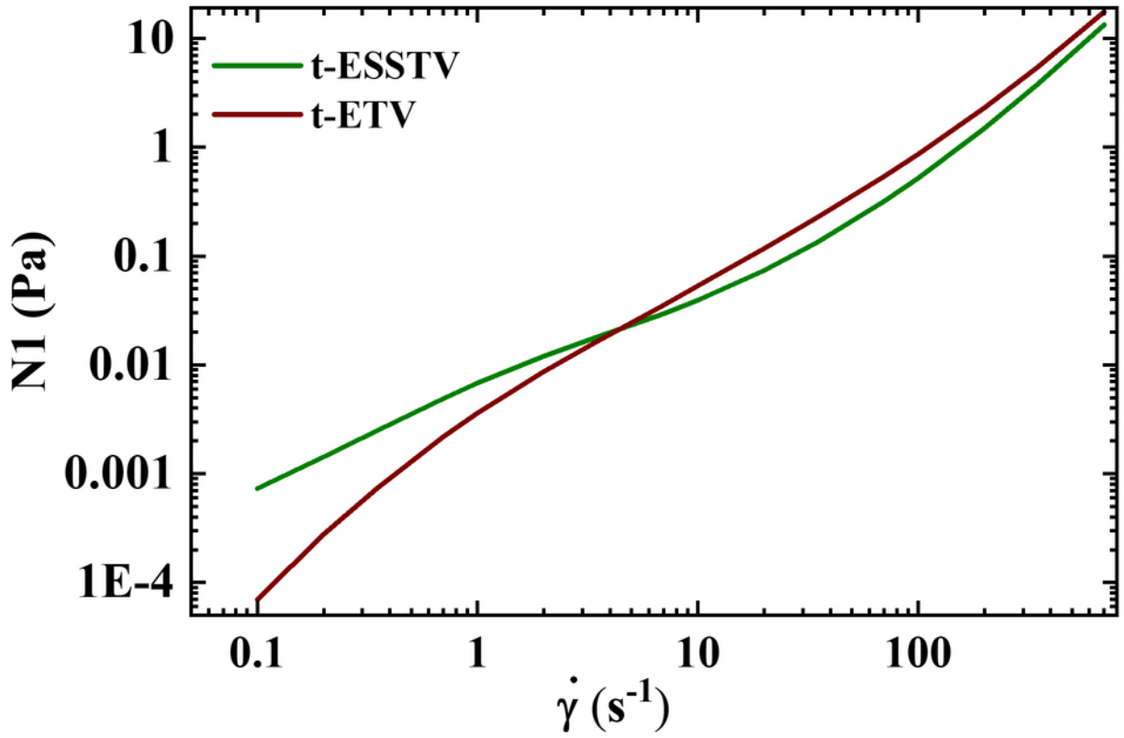

FIG. B1 N1 predictions of t-ESSTV and t-ETV for Donor3 (dataset3) [55].

Journal of Rheology

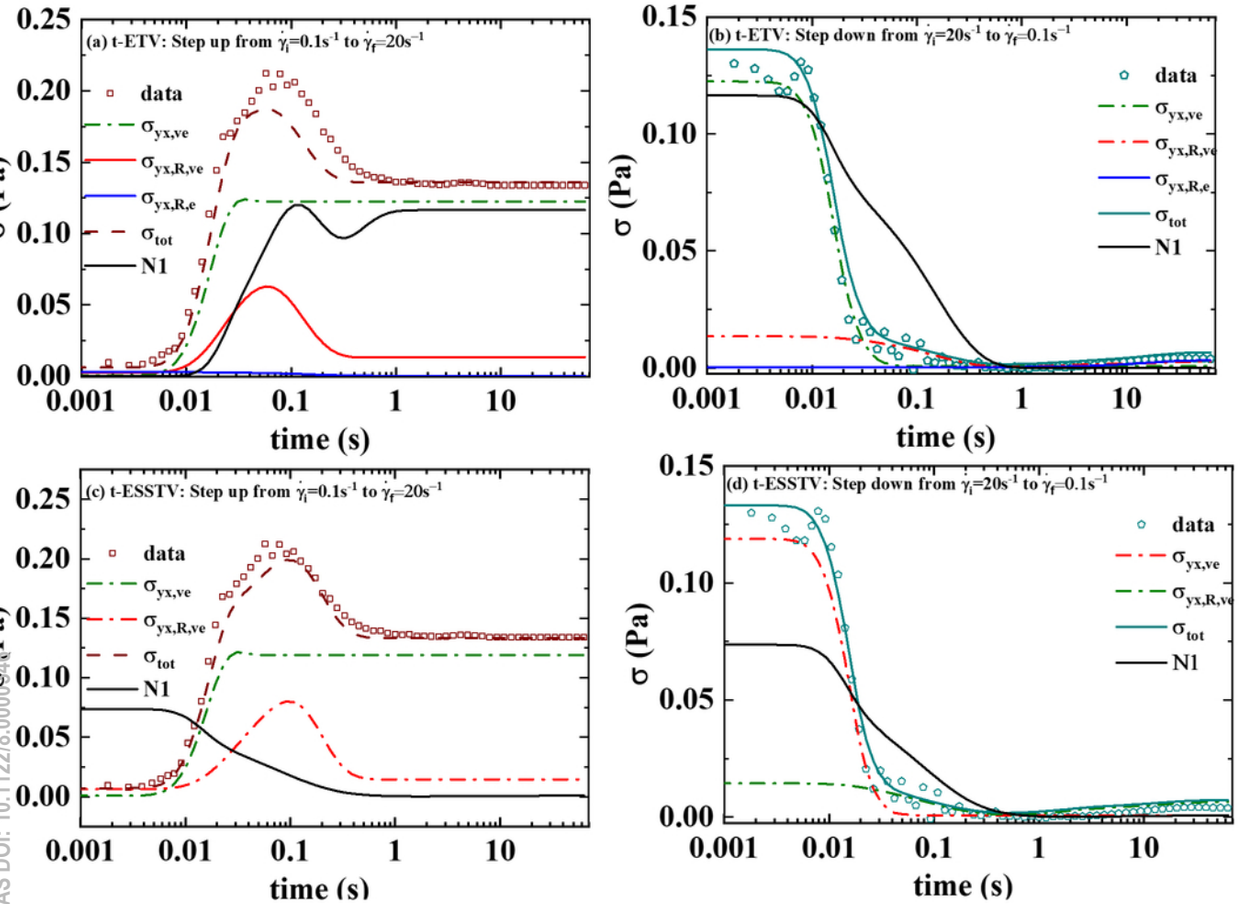

FIG. B2 (a,b) Contribution to total stress from plasma and RBCs (green dash-dot line), contribution to total stress from rouleaux (red solid line), contribution to total stress from elastic stress of rouleaux (blue solid line), total stress (wine dash line) and N1 predictions (black solid line) of t-ETV; and (c,d) contribution to total stress from plasma and RBCs (red dash-dot line), contribution to total stress from rouleaux (green dash-dot line), total stress (aqua line) and N1 predictions of t-ESSTV. (a,c) step up in shear rate from 0.1s^{-1} to 20s^{-1}; (b,d) step down in shear rate from 20s^{-1} to 0.1s^{-1}. (Data is maroon squares.) Donor3 (dataset3) [55].

Journal of Rheology

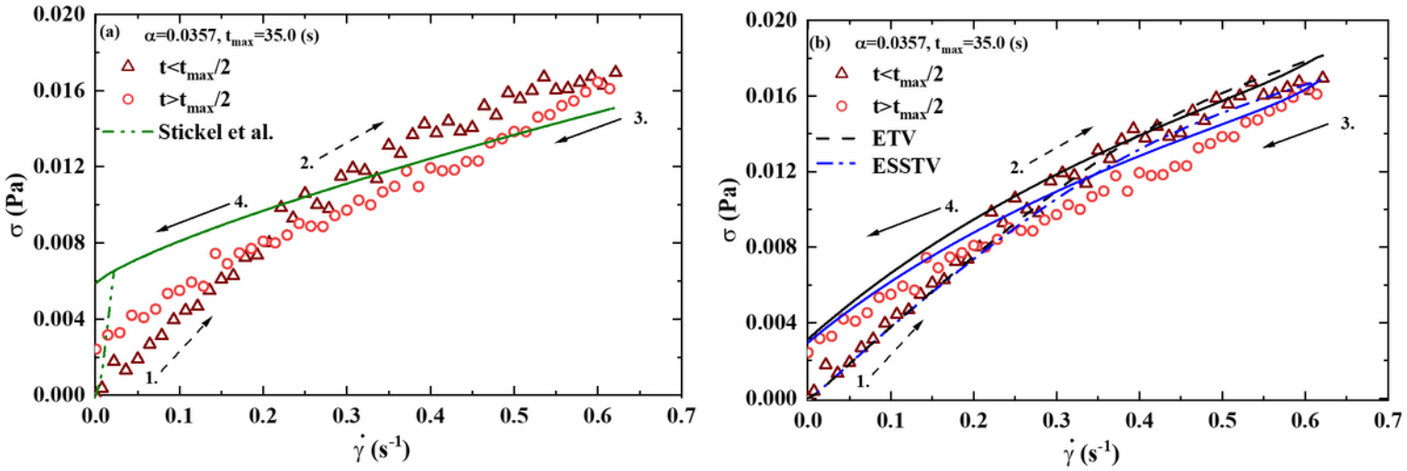

FIG. C1 Hysteresis loop for Donor 3 α=0.0357, t_{max}=35(s); data points as follows: $t<t_{max}/2$ maroon triangles, $t \geq t_{max}/2$ red circles; (a) Green line Stickel et al. [58] EVP model; and (b) Blue line ESSTV model; and black line ETV model. (Dashed lines represent $t < t_{max}/2$; solid lines represent $t \geq t_{max}/2$) (Numerals 1 – 4 are the stages of evolution of the hysteresis loop) (dataset3) [55], (Best fit parameter values: σ_{y0}=0.0058 (Pa); k=0.013; n=0.77; and G=1.64 (Pa)).

Journal of Rheology

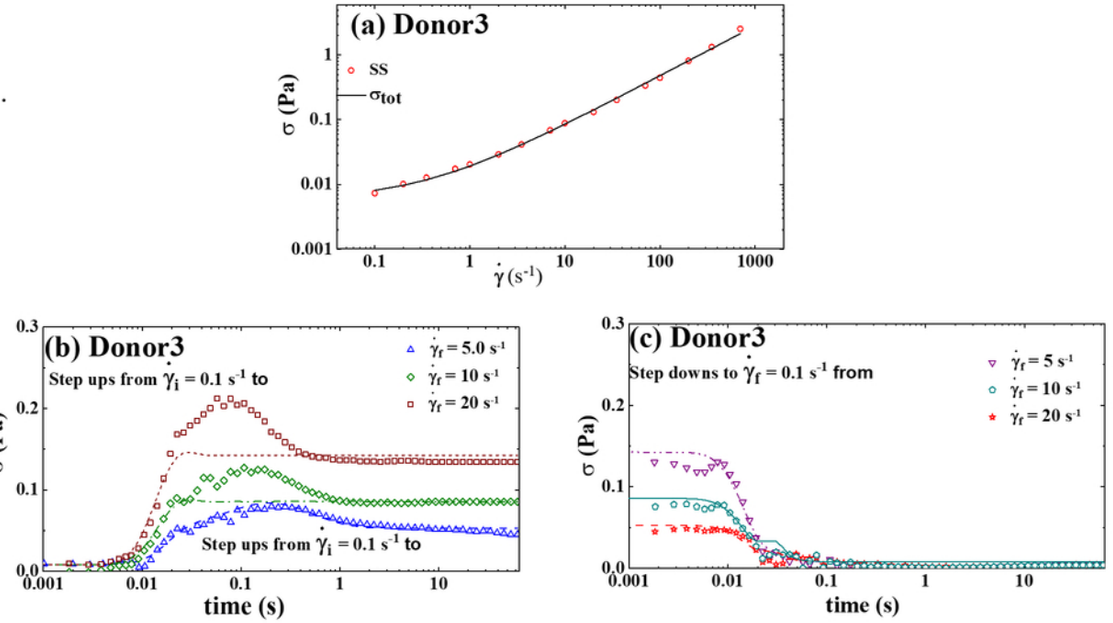

FIG. C2 Stickel et al. EVP model fit for (a) steady state human blood data; (b) set of 3 step-up in shear rate from of 0.1s-1 to 5, 10, and 20s-1; and (c) step-down in shear rate to of 0.1s-1 from 5, 10, and 20s-1 (Donor3) (dataset3) [55] (Best fit parameter values: σ_{y0}=0.0058 (Pa); k=0.013; n=0.77; and G=1.64 (Pa)